UCLouvain

FACULTE DES SCIENCES

Faculté des sciences

Arctic permafrost response to an extreme sea ice loss event in the CESM2-WACCM climate model

Author: **Antoine PAQUAY**
Supervisors: **François MASSONNET, Thierry FICHEFET**
Reader: **Michel CRUCIFIX**
Academic year 2024–2025
Master [120] en sciences géographiques, orientation climatologie

Abstract

The Arctic, where observed surface air temperatures have been warming nearly four times faster than the global average since 1979, is undergoing rapid transformations with profound environmental and socio-economic implications. This study examines the impacts of a major Rapid Sea Ice Loss Event (RILE) on Arctic permafrost using the CESM2-WACCM climate model under a high greenhouse gas emission scenario (SSP5-8.5). The simulated extreme RILE, characterized by a sea ice extent reduction of approximately 5 million square kilometers from 2031 to 2043, amplifies Arctic permafrost warming. Locally, permafrost temperature anomalies rise by up to 4°C per decade during winter at shallow depths, with an average winter warming rate that is three times faster than the climatological mean during the RILE period across Arctic permafrost regions (60–90°N). The warming signal penetrates to depths of about 10 meters, albeit with reduced intensity. The Nunavut, Chukotka, and Kara Sea regions are the most affected.

Changes in active layer thickness (ALT) and the depth of zero annual temperature amplitude (Dzaa) reveal distinct responses between warm and cold permafrost. Warm permafrost margins exhibit ALT increases exceeding 4 meters per decade, while colder permafrost regions show Dzaa increases of up to 20 meters per decade. However, some areas experience decreases in both ALT and Dzaa.

The permafrost response is driven by enhanced winter turbulent heat fluxes from the ocean to the atmosphere, warming adjacent lands. Additionally, atmospheric circulation anomalies result in colder or warmer air advection over permafrost regions. During summer, decreased cloud cover in some areas leads to increased solar radiation absorption by the ground. Correlations between surface condition changes and shallow ground temperature changes indicate that snow depth is the primary factor influencing the permafrost response during winter. Snow depth trend anomalies show localized increases of up to 40 cm per decade, particularly in the Chukotka region, contributing to complex patterns of surface energy exchange.

This study suggests that Arctic permafrost may be vulnerable to extreme climate forcing such as a RILE, offering insights into the mechanisms driving its degradation. These findings emphasize the need to address Arctic warming and its global climate feedbacks, including accelerated carbon release. Future research involving different models and scenarios would improve understanding of the potential permafrost response.

ChatGPT 4o was used in this master's thesis to improve the clarity, spelling, and grammar of the text.

Acknowledgments

First, I would like to thank my supervisors, François Massonnet and Thierry Fichefet, for their guidance and support throughout the course of my master's thesis. I am also thankful to PhD student Annelies Sticker, who provided assistance with the technical aspects of my work and offered insightful advice. Special thanks goes to Professor Sophie Opfergelt for taking the time to provide valuable feedback and guidance on the permafrost component of this research.

I am especially grateful to my grandparents, parents, and sisters for their continuous support throughout all these years of study, which were not always easy. In particular, I want to honor my late grandparents, Laure Franck and Roger Vanden Heede, who inspired my passion for nature and adventure. I deeply wish they could have seen me graduate and pursue what I love most: being in the wilderness.

Finally, I would like to thank my fellow students and professors from the University of Louvain, who provided me with a strong foundation as a geographer and climatologist. I am also grateful to those from the University of Oslo and the University Centre in Svalbard, who introduced me to the polar world, offering both theoretical knowledge and practical field experience in mainland Norway and Svalbard.

Contents

1 Introduction 1

2 Literature review 3

2.1 Arctic sea ice & Rapid Sea Ice Loss Events (RILEs) 3

2.2 Impacts of RILEs on the Arctic climate 6

2.3 Permafrost and its response to RILEs 8

3 Material and method 14

3.1 CESM2-WACCM climate model 14

3.2 RILEs and model assessment for sea ice extent and permafrost 17

3.3 Permafrost response and causes 19

4 Results 23

4.1 Model verification and RILE selection 23

4.2 Permafrost response 25

4.3 Drivers of the permafrost response 37

5 Discussion 43

6 Conclusion 46

Bibliography 54

Appendix 61

List of Acronyms

ADA	Arctic Dipole Anomaly
ALT	Active Layer Thickness
ASO	August-September-October
CCSM3	Community Climate System Model version 3
CESM2	Community Earth System Model Version 2
CLM3.5	Community Land Model version 3.5
CLM5	Community Land Model version 5
CMIP6	Coupled Model Intercomparison Project Phase 6
Dzaa	Depth of zero annual amplitude
ESGF	Earth System Grid Federation
FMA	February-March-April
GT10m	Ground Temperature at 10m
LAI	Leaf Area Index
LH	Latent Heat flux
LW	Longwave radiation
MJJ	May-June-July
MMGST	Mean Monthly Ground Surface Temperature (0.2m depth)
NDJ	November-December-January
NSIDC	National Snow and Ice Data Center
PV	Polar Vortex
RILEs	Rapid sea Ice Loss Events
SEB	Surface Energy Balance
SH	Sensible Heat flux
SIE	Sea Ice Extent
SLP	Sea Level Pressure
SND	Snow Depth
SO	Surface Offset
SST	Sea Surface Temperature
SSPs	Shared Socioeconomic Pathways
SW	Shortwave radiation
TAS	Surface Air Temperature (at 2m)
WACCM	Whole Atmosphere Community Climate Model

1 Introduction

The Arctic is undergoing rapid changes due to climate change, with surface air temperatures increasing nearly four times faster than the global average since 1979, as highlighted by Rantanen et al. (2022). This accelerated warming, known as Arctic Amplification, results from a combination of feedback mechanisms. Climate models project that the Arctic will face substantial and potentially irreversible transformations in the coming decades, particularly during winter. These include accelerated sea ice loss and permafrost thaw, which may release large quantities of methane and carbon dioxide (AMAP 2021, IPCC 2023).

Under high greenhouse gas emission scenarios, the Arctic Ocean is projected to be sea ice-free during summer by mid-century. Even with significant emission reductions, warming and sea ice loss will likely persist due to the cumulative effects of existing greenhouse gas concentrations (AMAP 2021, IPCC 2023). Summer sea ice, particularly at its minimum extent in September, exhibits nonlinear behavior in both observations and models. Minima were observed in 2007 and 2012 (Figure 1.1), and climate models project Rapid Sea Ice Loss Events (RILEs) that are typically more prolonged and intense than these isolated observed events. Multiple definitions of RILEs exist; one, based on Auclair & Tremblay (2018), describes a RILE as a period with a Sea Ice Extent (SIE) decline rate exceeding 0.3 million square kilometers per year over at least 4 years using the five-year rolling mean. Climate models suggest such events will become more frequent and intense by mid-century, potentially accelerating the timeline for a sea ice-free Arctic Ocean in summer (Holland et al. 2006, Döscher & Koenigk 2013, Paquin et al. 2013).

Sea ice regulates heat and water vapor exchange between the ocean and atmosphere, influencing nearby permafrost and the global climate system (Serreze & Barry 2014). RILEs can impact permafrost, as demonstrated by Lawrence et al. (2008) using earlier climate models. Their study showed that RILEs could warm permafrost soils 3.5 times faster than the century-scale average, accelerating thaw. Given the vast carbon stores in permafrost, its accelerated thaw could amplify global warming. Thawing permafrost also poses serious risks to infrastructure, hydrology, ecology, and slope stability, with wide-ranging socio-economic and environmental consequences (Marshall 2012, Barry 2018).

Since the work of Lawrence et al. (2008), no other research has specifically examined the impact of RILEs on permafrost. However, recent studies, such as Sticker (2022), have highlighted the need for further research on this topic, providing an inventory of events in advanced climate models from the Coupled

Model Intercomparison Project Phase 6 (CMIP6). These models show improved simulations of Arctic September sea ice and offer slight enhancements in representing permafrost dynamics (Burke et al. 2020, Notz & Community 2020). Although modest, these improvements provide an opportunity to revisit and deepen our understanding of RILE impacts on permafrost.

This master's thesis aims to investigate permafrost response during a RILE using a CMIP6 model with advanced soil and atmospheric representations. The study will evaluate whether an extreme RILE generates a measurable permafrost response and identify the mechanisms driving this signal. The CESM2-WACCM (Community Earth System Model Version 2 coupled with the Whole Atmosphere Community Climate Model Version 6) model was selected for its deep soil profile and detailed atmospheric representations, including the stratosphere.

The central hypotheses are: (1) an extreme RILE will result in significant permafrost warming, particularly near sea ice loss regions, driven by enhanced heat fluxes from the ocean to the atmosphere, primarily via turbulent fluxes; and (2) changes in snow depth over permafrost lands during the RILE will strongly influence the permafrost response.

The extreme conditions chosen for this study, a strong greenhouse gas emission scenario combined with an extreme RILE, are expected to produce a pronounced permafrost response. These findings aim to contribute to a framework for further investigations using additional models and scenarios, enhancing our understanding of accelerated permafrost thaw and its potential implications for carbon release.

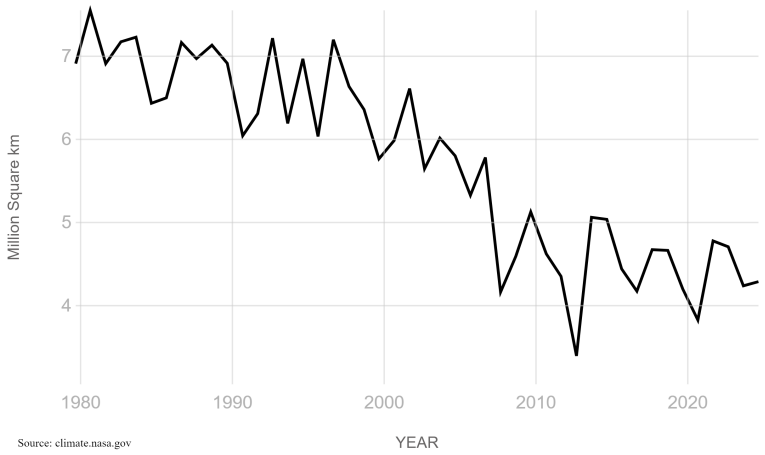


Figure 1.1: Arctic September sea ice extent based on satellite observations. Credit: NSIDC/NASA

2 Literature review

This chapter establishes the foundations for understanding sea ice and RILEs, including their causes, consequences, and potential impacts on permafrost. The drivers and impacts of RILEs are often intertwined, complicating the distinction between cause and consequence. In addition to studies specific to RILEs, general research on the impacts of sea ice loss on the Arctic climate is reviewed. These broader studies provide useful context, as phenomena observed under general sea ice loss are likely amplified during RILEs. An introduction to permafrost is also included to explain how changes in surface conditions caused by RILEs can affect its temperatures. Finally, the study by Lawrence et al. (2008), which examined the impact of RILEs on permafrost, is reviewed.

2.1 Arctic sea ice & Rapid Sea Ice Loss Events (RILEs)

Arctic sea ice is an important component of the climate system, influencing weather patterns, ocean circulation, coastal stability, ecosystems, and planetary albedo. Its maximum extent (defined as areas with an ice concentration exceeding 15%) is in March and minimum in September, with 1979 to 2011 average values of $15.5 \times 10^6 \text{km}^2$ and $6.6 \times 10^6 \text{km}^2$, respectively (Marshall 2012).

The World Meteorological Organization classifies sea ice into stages based on thickness, starting with new ice (less than 10 cm), progressing to young ice (10–30 cm), followed by first-year ice (over 30 cm), which completely melts during the summer season, and multiyear ice (2–4 meters), which survives multiple melting seasons (NSIDC n.d.*a*).

The freezing point of seawater is approximately -1.8°C due to its salinity. The presence of dissolved salts lowers the freezing point of seawater with typical values of 0.054°C per parts per thousand. (Marshall 2012, Barry & Gan 2021). As the density of salty water increases while approaching the freezing point, the freezing point temperature needs to be reached by the upper 100 to 150 meters of the water column to allow the surface to freeze. This makes the formation of sea ice a slow and gradual process compared to freshwater ice (NSIDC n.d.*a*).

The initial stage of sea ice formation is small needle-like crystals known as frazil ice. These crystals accumulate into thin sheets, forming grease ice in calm waters, which later develops into a thicker layer called nilas. The sea ice formation continues with direct crystal growth at the bottom. In rougher conditions, frazil ice

forms slushy, circular pancakes with raised edges due to collisions. This pancake ice will consolidate, and the growth will also continue from the bottom (NSIDC n.d.*a*). Sea ice mechanics (convergence, compression, and rafting) can lead to thicker ice, with, for instance, pressure ridges of up to 20 m (Marshall 2012). Sea ice thickness can be impacted by the snowpack, as it acts as an insulator, leading to thinner ice during winter and thicker ice during summer. Important snow depth on thin ice may weigh it down, causing flooding on top of the ice with salty water. In summer, melting snow creates melt ponds on the ice surface, which absorb more heat and expand (NSIDC n.d.*a*).

As sea ice forms, the salt contained in the water is forced out and concentrated saltwater droplets called brine are trapped in pockets within the ice or rejected into the ocean. Thus, surface water where sea ice forms becomes saltier and plays an important role in ocean circulation. These brine pockets within the ice decrease over time as gravity, compression, and melting processes push the salt out (NSIDC n.d.*a*).

Sea ice undergoes continual motion due to winds, currents, and ocean surface tilt. This movement leads to the formation of dynamic features such as leads, narrow cracks allowing heat exchange and biological activity, and polynyas, larger open-water areas sustained by warm water upwelling or persistent winds. These features influence local climate, wildlife habitats, and ocean circulation (NSIDC n.d.*a*).

Satellite observations since 1979 have documented a decline in SIE, thickness, and volume, with the most pronounced reductions occurring during summer months (Holland et al. 2006, Jahn et al. 2024). Sea ice loss results from a combination of anthropogenic warming, natural climate variability, and feedback mechanisms such as the ice-albedo effect (Holland et al. 2006, Rieke et al. 2023). Snow and ice, with their high albedo, reflect most of the incoming solar radiation, providing a cooling effect. As the cryosphere components experience a decline in extent and volume under current climate change, darker surfaces like open water replace these reflective surfaces, absorbing more solar radiation and leading to further warming (Serreze & Barry 2011, Rantanen et al. 2022).

Holland et al. (2006), using the Community Climate System Model version 3 (CCSM3), identified abrupt sea ice losses referred to as RILEs, which have since been simulated in numerous climate models. Observed SIE minima, such as those in 2007 and 2012, helped researchers analyze preconditioning factors of abrupt sea ice declines that could potentially trigger RILEs in the future (Döscher & Koenigk 2013, Paquin et al. 2013). As sea ice continues to thin, climate models suggest that RILEs

could occur by the mid-21st century and will increase in frequency and intensity due to the combined effects of internal variability and ongoing warming (Döscher & Koenigk 2013, Rieke et al. 2023). These events may accelerate the Arctic's transition to a summer sea ice-free state, emphasizing the need to understand their mechanisms and, in this work, their impacts.

Definitions of RILEs vary across studies. In addition to the definition from Auclair & Tremblay (2018) described in the introduction, Döscher & Koenigk (2013) and Rieke et al. (2023) defined RILEs based on sea ice loss thresholds, such as exceeding 1.2 million km^2 in a single year or trends surpassing seven times the historical rates. Other definitions use rolling mean trends. Holland et al. (2006) and Paquin et al. (2013) describe RILEs as periods with a 5-year rolling mean of sea ice extent declining at a rate of at least -0.5 million km^2 per year, sustained by annual losses exceeding 0.15 million km^2. Lawrence et al. (2008) characterized RILEs as 5–10-year periods with sea ice extent losses approximately four times greater than the long-term average trend. In this master's thesis, an adapted method by Sticker (2022) based on the definition of Holland et al. (2006) is used to identify RILEs.

Causes of the RILEs

RILEs are triggered by a combination of sea ice thinning, oceanic heat transport, and atmospheric anomalies, with feedback mechanisms amplifying their intensity. The relative importance of these drivers varies across Arctic regions and individual events (Paquin et al. 2013, Rieke et al. 2023).

Long-term warming has reduced the prevalence of thicker, older, multi-year ice, rendering the ice pack more vulnerable to forcing from oceanic and atmospheric anomalies. Climate models consistently show thinning ice as a precursor to RILEs (Holland et al. 2006, Paquin et al. 2013). Episodic anomalous oceanic heat transport into the Arctic, linked to changes in ocean currents and wind patterns, often precedes RILEs. Warm water inflows from the Atlantic and Pacific Oceans enhance basal melting of sea ice (Paquin et al. 2013, Rieke et al. 2023).

Atmospheric circulation anomalies, such as the positive phase of the Arctic Dipole Anomaly (ADA), with a high-pressure system over the Arctic Ocean on the American side and a low-pressure system on the Eurasian side, lead to enhanced transpolar drift, increasing sea ice export to warmer regions and accelerating melt. Additional factors, such as warmer air advection and reduced summer cloud cover, amplify radiative heating of the ice and ocean surface, preconditioning the system for a RILE (Döscher & Koenigk 2013, Paquin et al. 2013).

Feedback loops play a dual role in triggering and intensifying RILEs. The ice-albedo feedback accelerates ice melt during periods of sufficient sunlight and contributes to oceanic heat storage, hindering seasonal ice recovery (Döscher & Koenigk 2013, Paquin et al. 2013). Other feedbacks include changes in Arctic Ocean stratification and cloud properties, which modulate heat fluxes. The freshening of surface waters due to ice melt reduces vertical mixing, trapping heat in the upper ocean layer. Reductions in sea ice alter atmospheric moisture and temperature profiles, leading to increased cloud cover and atmospheric humidity in some regions, trapping outgoing longwave radiation (Goosse et al. 2018, Rieke et al. 2023).

2.2 Impacts of RILEs on the Arctic climate

The impacts are divided into two interconnected components: near-surface changes over the ocean and permafrost lands, which directly affect the permafrost, and atmospheric circulation changes, which influence the near-surface response.

During RILEs, surface air temperatures at 2 m (TAS) can increase up to 10°C per decade during November and December above the Arctic Ocean, according to Paquin et al. (2013). This warming is closely associated with changes in the net surface energy budget rather than the exact timing of minimum sea ice extent. The delay arises because the open ocean, exposed by sea ice loss during summer, absorbs more solar radiation and then releases the accumulated heat into the atmosphere primarily during early winter, when colder air masses increase turbulent heat fluxes. This contrasts with autumn, when sea ice loss peaks but TAS anomalies are less pronounced (Paquin et al. 2013).

TAS increases over land vary spatially and seasonally, with the largest anomalies observed in December (approximately 3.3°C per decade) and smaller increases in May (around 1.3°C per decade). The discrepancy between TAS anomalies above the ocean and land raises questions about atmospheric heat transport mechanisms. While surface winds are expected to advect warmer air from the ocean to adjacent lands, leading to similar TAS anomalies, studies reveal complexities in vertical heat transfer. For instance, Paquin et al. (2013) demonstrated that during RILEs, the low-level temperature inversion over the Arctic Ocean weakens or even disappears locally due to greater turbulent heat fluxes from the ocean, allowing heat to propagate vertically. This weakens horizontal advection, explaining the more subdued warming signals over adjacent lands(Paquin et al. 2013).

Cloud cover anomalies during RILEs influence the radiation budget. During autumn, increased low-cloud cover due to greater evaporation traps downward

longwave (LW) radiation, delaying ice recovery. Conversely, in winter, reduced total cloud cover caused by an anticyclonic pattern allows for enhanced outgoing LW radiation, countering warming trends. However, liquid water within clouds slightly increases during winter, providing minor radiative forcing (Vavrus et al. 2011).

Changes in cold-season precipitation, including snowfall and rainfall, further influence land surface conditions. Liu et al. (2024) demonstrated that observed reduced Arctic sea ice coverage increases evaporation from marginal seas, driving moisture into high-latitude regions and leading to extreme snowfall events locally. However, as Arctic warming progresses, a shift toward rain-dominated precipitation is anticipated.

RILEs impact atmospheric circulation at both surface and upper levels. As described by Liang et al. (2024) using CESM2-WACCM, Arctic sea ice loss weakens the stratospheric polar vortex (PV) during early winter, with the extent of weakening proportional to the magnitude of sea ice loss. Enhanced upward propagation of Rossby waves disrupts the stratospheric mean flow, driving this weakening. The weakened PV subsequently influences tropospheric circulation during late winter and spring, amplifying surface impacts (Liang et al. 2024).

The atmospheric signal from sea ice loss propagates upward in early winter, peaking in the stratosphere by mid-December. It descends to the troposphere by January, altering zonal wind patterns, storm tracks, and precipitation. These changes are associated with a more negative phase of the Arctic Oscillation, characterized by a wavier jet stream that facilitates exchanges of warmer and colder air masses between the Arctic and mid-latitudes (Figure 2.1) (Chripko et al. 2021).

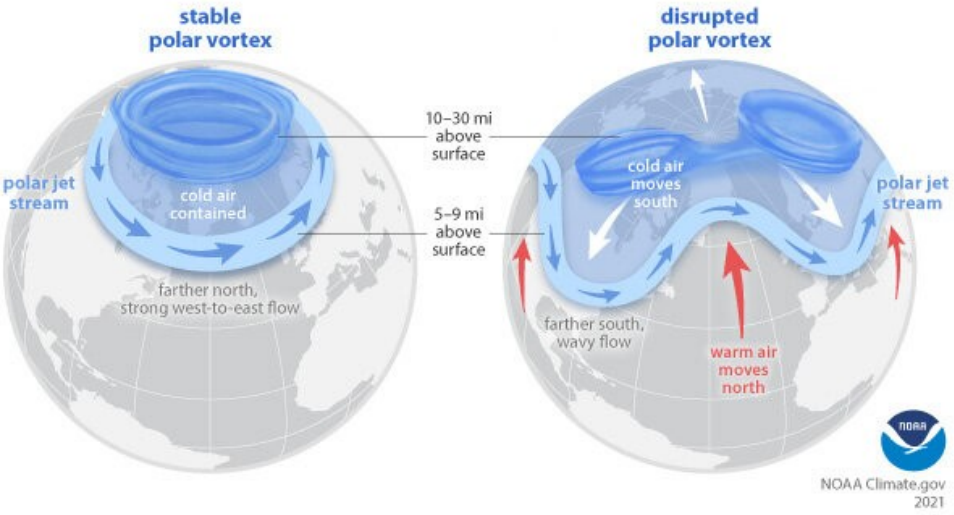


Figure 2.1: Impacts of the polar vortex stability on the jet stream behavior and warm/cold air advection. Credit: NOAA Climate.gov

2.3 Permafrost and its response to RILEs

This section explores the characteristics of permafrost, the role it plays within the Earth's climate system, and its potential responses to the forcing introduced by RILEs. By describing state variables such as the Active Layer Thickness (ALT) and Depth of Zero Annual Amplitude (Dzaa) for the soil temperature, we establish a framework for evaluating permafrost response under the influence of a RILE. Additionally, the Surface Energy Balance (SEB) is introduced as a tool for understanding energy transfer processes between the atmosphere and the surface (lower boundary of the atmosphere) affecting permafrost. Finally, findings from the study by Lawrence et al. (2008) on RILE-induced permafrost impacts are discussed, forming the basis of this thesis.

Characteristics of permafrost

Permafrost, as defined by the International Permafrost Association, is «ground (soil or rock, including ice or organic material) that remains at or below 0°C for at least two consecutive years.» Covering approximately 25% of the Northern Hemisphere's exposed land, permafrost extends globally over 14–16 million km^2 and can be classified into four coverage categories: continuous (over 90%), discontinuous (50–90%), sporadic (10–50%), and isolated patches (less than 10%) (Figure 2.2)

(Westerveld et al. 2023). Its depth can reach up to 1,000 meters in regions such as Siberia (Barry 2018).

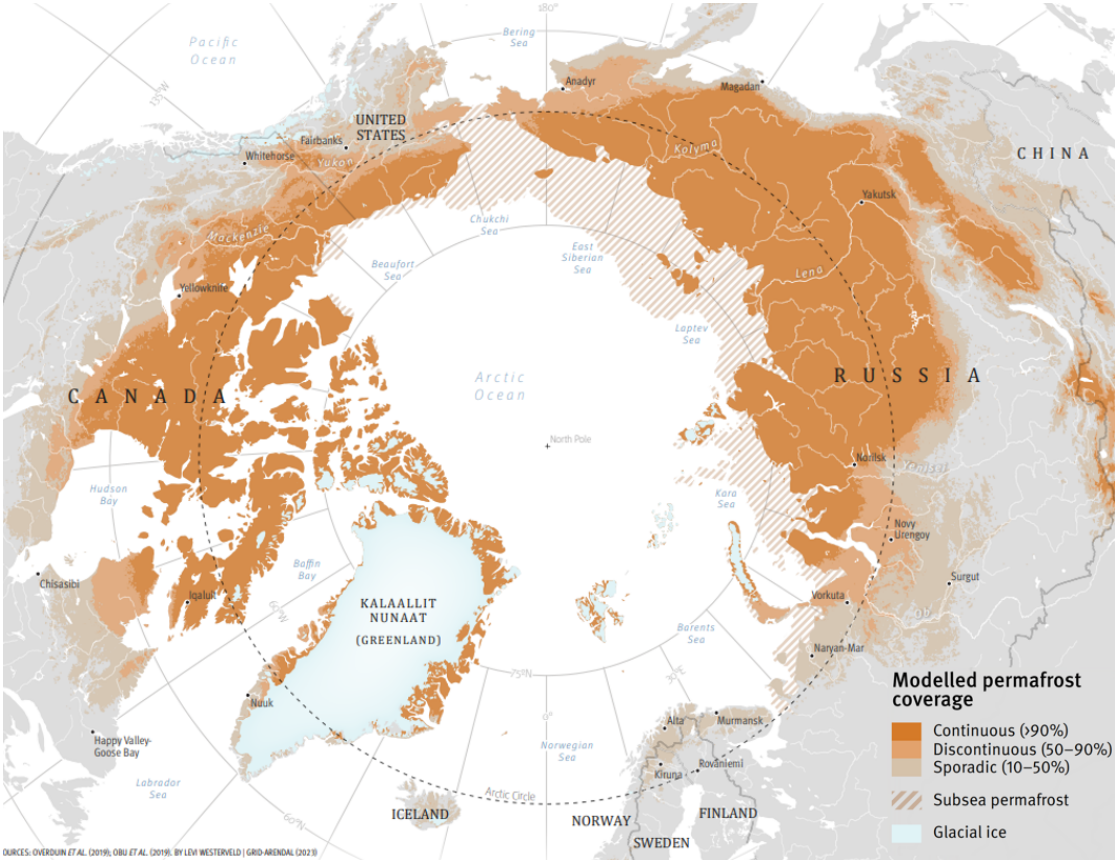


Figure 2.2: Current modelled Arctic permafrost coverage. Credit: Westerveld et al. (2023)

Permafrost represents a substantial carbon reservoir, storing 2.5 times more carbon than the atmosphere. Upon thawing, it has the potential to release significant amounts of greenhouse gases, including methane (CH_4) and carbon dioxide (CO_2). Even if increased plant growth absorbs a portion of these emissions, it won't fully offset them, posing a potential risk of amplifying climate change through positive feedback mechanisms (Marshall 2012, Barry 2018, NSIDC n.d.*b*). Despite its high warming potential, methane has a shorter atmospheric lifetime compared to CO_2, approximately a decade versus hundreds to thousands of years for CO_2 (Huissteden 2020, NASA/JPL-Caltech 2023).

Temperature is the primary determinant of permafrost occurrence. The mean annual air temperature isotherms of -8°C and -1°C delineate the limits for continuous

and discontinuous permafrost zones, respectively. Within regions of continuous permafrost, localized unfrozen ground, known as taliks, may occur, potentially influencing heat transfer processes and permafrost degradation (Van Vliet-Lanoë 2014).

The active layer (Figure 2.3) refers to the uppermost permafrost layer that undergoes seasonal thawing and refreezing. Its depth can vary from as little as 10 cm to over 4 meters, influenced by factors such as vegetation cover, snow insulation, topography, soil type, and albedo (Huissteden 2020). ALT changes directly affect carbon release from the soil, making it an important parameter for understanding permafrost responses to surface condition changes.

The Dzaa (Figure 2.3) is another useful indicator, representing the depth below which temperature fluctuations due to seasonal variations are no longer observed. Changes in the Dzaa are indicative of long-term thermal trends, as opposed to rapid surface changes that primarily affects the ALT (Marshall 2012). These indicators together provide a comprehensive picture of permafrost dynamics, offering a means to assess the lasting impacts of RILEs.

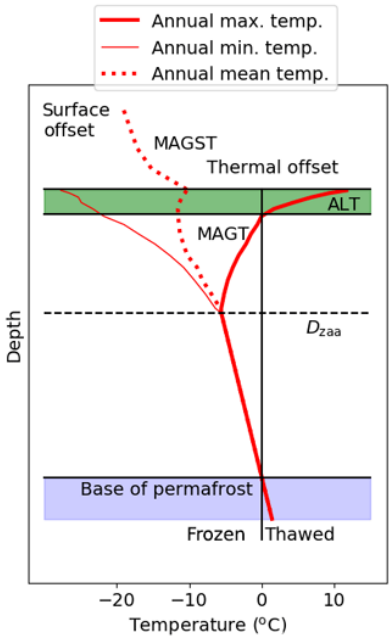


Figure 2.3: Annual temperature variations from the surface to below the permafrost, showing the Active Layer Thickness (ALT) indicating seasonal thaw depth and the Depth of zero annual amplitude (Dzaa) marks the depth where seasonal temperature fluctuations cease. Credit: Burke et al. (2020)

The permafrost state is mainly governed by the transfer of energy between the atmosphere and the ground, a process best understood through the SEB which is next described using Huissteden (2020). The basic SEB (W/m^2) equation can be expressed as:

$$SEB = SW_{\text{net}} + LW_{\text{net}} - LH - SH \tag{1}$$

where:

- SW_{net}: Net downward shortwave radiations in W/m^2.
- LW_{net}: Net downward longwave radiations in W/m^2.
- LH: Latent heat flux, energy transfer between the surface and the atmosphere associated with phase changes of water (e.g., evaporation or condensation) in W/m^2, positive when upward.
- SH: Sensible heat flux, energy transfer driven by temperature gradients between the surface and the atmosphere in W/m^2, positive when upward.

To understand the SEB, it is important to explore the effects of snow, vegetation, and water transport, which influence the permafrost dynamics. These factors influence energy exchange processes at the ground surface and determine how permafrost responds to external climatic and environmental forcings.

Vegetation impacts the ground energy budget through interactions with incoming and outgoing SW and LW radiations, influencing the energy reaching the surface. Vegetation also contributes to turbulent heat fluxes, including sensible and latent heat exchange. Additionally, vegetation modifies surface roughness, altering wind patterns and reducing snow drift(Van Vliet-Lanoë 2014, Huissteden 2020).

Snow cover plays a central role in the SEB of permafrost due to its dual properties of high albedo and thermal insulation. Thick snow cover acts as a thermal shield, preserving residual summer warmth and insulating the ground from extreme winter cold. Conversely, a thin layer of snow reflects solar radiation while allowing heat exchange between colder winter air and the warmer ground. In spring and summer, melting snow exposes the soil to solar radiation, potentially increasing the ALT as the ground absorbs more heat (Zhang 2005, Van Vliet-Lanoë 2014).

Water transport also influences the thermal state of permafrost. Liquid water from ground ice melt, snow melt, glacier runoff, and rainfall redistributes heat and moisture within the permafrost system. This occurs through both horizontal and vertical pathways, altering the ground's properties (Marshall 2012).

Thermal properties of the ground, such as thermal conductivity, heat capacity, and thermal diffusivity, govern how temperature signals propagate through the soil. These properties vary seasonally and regionally due to changes in moisture content, soil type and phase transitions of water, introducing complexities in understanding permafrost responses (Marshall 2012). However, this study focuses on changes in soil frozen and liquid water contents to highlight potential latent heat impacts on the signal, rather than analyzing these thermal properties in detail.

Impacts of RILEs on permafrost

The specific impacts of RILEs on permafrost have been examined in the work of Lawrence et al. (2008) using the CCSM3 and its Community Land Model (CLM3.5). One key finding of this study is the identification of amplified land warming during RILEs, occurring at rates 3.5 times greater than typical 21st-century trends. Specifically, land temperatures increase at rates of 1.60°C per decade during RILEs, compared to 0.46°C per decade during non-RILE periods. This warming is most pronounced along Arctic coastlines, with TAS increases of up to 5°C per decade extending up to 1,500 kilometers inland (Figure 2.4). Seasonal patterns display warming peaks in autumn and early winter.

While colder permafrost exhibits greater resilience to immediate warming impacts, the additional heat gained during RILEs increases its long-term vulnerability to thawing. Over time, even small increases in soil temperature lead to important changes in permafrost dynamics, particularly as subsurface heat propagated deeper into the ground. Their study demonstrates that heat storage during RILEs amplifies long-term warming effects, posing risks to colder permafrost zones that were previously considered stable (Lawrence et al. 2008).

Since the study by Lawrence et al. (2008) using the land model CLM3.5, the updated version, CLM5.0, has been developed. This latest version is the land module of the CESM2-WACCM climate model used in this study. Numerous improvements have been made in permafrost modeling, vegetation processes, and snow dynamics (Lawrence et al. 2020).

The CLM5.0 version incorporates spatially variable soil thicknesses, replacing the uniform soil depth used previously. The soil structure was refined to include 20 layers, reaching depths of up to 49.56 m, with higher resolution in the top 3 m, compared to the 10 layers and depths of up to 3.43 m in version 3.5. Thermal dynamics were advanced by introducing processes like cryoturbation. Snow modeling improvements include an increase in the number of snow layers from

5 to 12 and the capacity to simulate firn in persistently snowy regions. Refined snow density calculations now incorporate both temperature and wind influences, ensuring better representation of compaction processes. These are just a few of the numerous enhancements made (Lawrence et al. 2020, Oleson et al. 2007).

In conclusion, the literature review demonstrates the potential impacts of RILEs on permafrost and highlights the need for continued research. Understanding the processes driving permafrost degradation during RILEs is essential for anticipating the broader consequences of Arctic climate change. The findings of Lawrence et al. (2008) provide a basis of RILE-induced permafrost responses, emphasizing the interconnectedness of sea ice dynamics, terrestrial climate, and permafrost health. Given the improvements in the Community Land Model discussed above, this study aims to analyze the permafrost response during an extreme RILE using updated models, building on findings from previous studies.

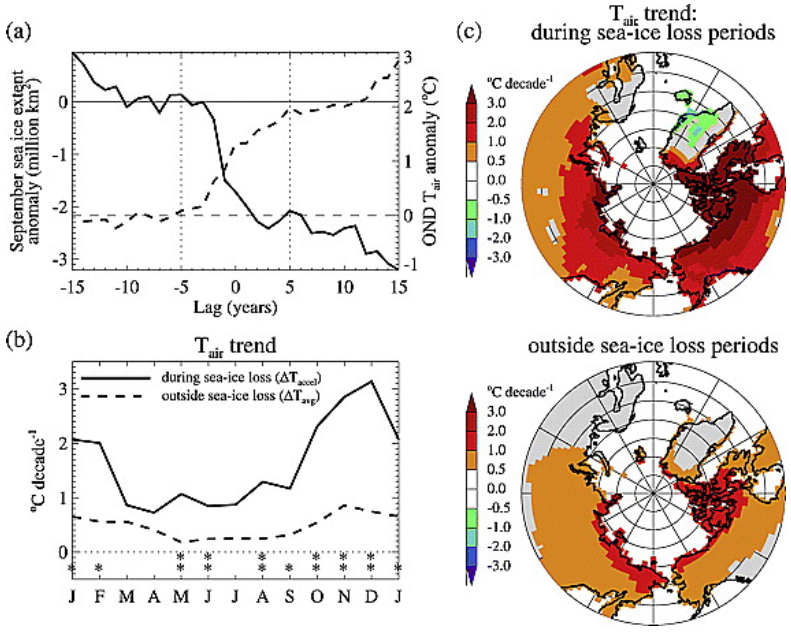


Figure 2.4: « (a) Composite anomaly time series of September sea ice extent (solid line) and OND Tair (dashed line) over Arctic land area (65°–80°N, 60°–300°E). Composites are formed by averaging nine 31-yr anomaly time series. Each of the nine time series are centered about the mid-point of a CCSM3 rapid sea ice loss event (lag 0 years) and are anomalies from the lag 10 to 5 year mean. (b) Average monthly Arctic land air temperature trends during rapid sea ice loss periods and outside sea ice loss periods. The difference in trends are statistically significant at the 90% (single asterisk) and 95% (double asterisk) levels. (c) Maps of air temperature trends for OND during and outside abrupt sea ice loss periods.» (Lawrence et al. 2008) Credit: Lawrence et al. (2008)

3 Material and method

The first step involves selecting a model from the CMIP6 project that satisfies several criteria. The chosen model must exhibit an extreme RILE, provide sufficiently detailed and deep soil temperature data to enable the use of the Dzaa for evaluating long-term impacts, and include atmospheric profiles extending into the stratosphere to account for stratosphere-troposphere interactions.

The CESM2-WACCM climate model from the CMIP6 project meets these criteria. Its characteristics are described in the following section, beginning with an introduction to the CMIP6 project, followed by an explanation of CESM2-WACCM and the selected Shared Socioeconomic Pathway (SSP). Subsequently, the methods used to evaluate the model's capability to simulate sea ice extent and permafrost are detailed. Finally, the methodology for selecting a RILE, analyzing its impacts on the climate and permafrost, and investigating the underlying causes of simulated signals in permafrost is described.

3.1 CESM2-WACCM climate model

Coupled Model Intercomparison Project Phase 6 (CMIP6)

The CMIP6 project is an initiative in climate science, providing a comprehensive framework for the systematic evaluation and intercomparison of Earth system models. Coordinated by the World Climate Research Programme, its design and outputs are useful for advancing our understanding of past, present, and future climate dynamics. CMIP6 supports global climate assessments, such as the IPCC reports, and guides policy decisions (Eyring et al. 2016).

CMIP6 investigates how the Earth system responds to forcings, addresses the impact of model biases, and explores uncertainties in projections. It employs standardized experiments as baselines for inter-model comparisons and incorporates specialized Model Intercomparison Projects (MIPs) to study specific processes, including land-atmosphere coupling, cryosphere dynamics, and biogeochemical feedbacks (Eyring et al. 2016, Danabasoglu et al. 2020).

One notable advantage of CMIP6 is its emphasis on data standardization and accessibility. Model outputs are archived and disseminated via the Earth System Grid Federation (ESGF), ensuring consistent formats and metadata across datasets. This facilitates global collaboration and analysis by researchers. An integral feature

of CMIP6's data organization is the "ripf" identifier, encoding specific information about model runs. The "r" represents the realization or ensemble member, denoting multiple simulations with slightly varied initial conditions to assess variability. The "i" denotes the initialization method, distinguishing how simulations are started. The "p" indicates the physics version, reflecting variations in model configuration or parameterization schemes, while the "f" specifies the forcing scenario used (Eyring et al. 2016). Data from CMIP6 are freely available via the ESGF[1] website.

CESM2-WACCM – Model overview and capabilities

The CESM2 is a state-of-the-art Earth system model developed by the National Center for Atmospheric Research (NCAR). Designed to simulate complex interactions between the atmosphere, land, ocean, cryosphere, and biosphere, CESM2 offers a robust framework to investigate permafrost responses to RILEs (Danabasoglu et al. 2020).

CESM2-WACCM, a specialized configuration, couples the WACCM6 module to account for stratosphere-troposphere coupling (Gettelman et al. 2019). CESM2-WACCM comprises various modules to simulate the different climate system components, summarized in Table 3.1.

The WACCM6 atmospheric module simulates processes from the surface to approximately 140 km, encompassing the troposphere, stratosphere, mesosphere, and lower thermosphere. This study utilizes atmospheric data spanning from 1000 hPa to 1 hPa across 19 levels. WACCM6 integrates comprehensive parameterizations for chemistry and aerosols, enabling the study of phenomena such as stratospheric-tropospheric interactions, sudden stratospheric warming events, and ozone dynamics (Gettelman et al. 2019, Davis et al. 2023).

Some of the features of the land module CLM5 are already described in the literature review. Additionally, CLM5 integrates heat and water transfer systems to simulate freeze-thaw processes which is important in permafrost state changes. Its snow thermal module captures snow's insulating effects, which play a key role in regulating soil temperatures in permafrost regions. CLM5 also incorporates a dynamic vegetation module that simulates changes in surface energy fluxes and their effects on permafrost. As well as hydraulic redistribution, a feature that accounts for water movement within soil layers (Lawrence et al. 2019).

The sea ice component, CICE5.1, simulates the thermodynamic and mechanical

[1] `https://aims2.llnl.gov/search/cmip6/`

behavior of sea ice. High-resolution models effectively capture sea ice thickness, concentration, and variability, essential for understanding feedbacks between sea ice loss and atmospheric circulation. Studies using CESM2 demonstrate improved performance in replicating historical sea ice trends and projecting changes compared to CMIP5 (DeRepentigny et al. 2020).

Module	Horizontal Resolution	Vertical Layers	Vertical Extent	Sources
Atmospheric Module (WACCM6)	100 km	88	~140 km (lower thermosphere)	Gettelman et al. (2019) ; Danabasoglu et al. (2020)
Land Module (CLM5)	100 km	20	Soil extends to ~50 meters depth	Lawrence et al. (2019)
Sea Ice Module (CICE5.1)	100 km	5-7	Ice thickness: ~2-5 m	DeRepentigny et al. (2020)
Ocean Module (POP2)	100 km	60	Extends to ~6 km depth	Danabasoglu et al. (2020)

Table 3.1: CESM2-WACCM characteristics.

Shared Socioeconomic Pathways (SSPs)

As outlined earlier, CMIP6 models employ various experiments to explore climate dynamics. To investigate the potential impact of RILEs on permafrost, it is convenient to select a scenario with an important anthropogenic forcing. Such a scenario is more likely to exhibit strong RILEs, resulting in a pronounced signal in the permafrost, which facilitates the analysis. The SSP5-8.5 scenario represents a high-emission pathway with significant forcing. The following paragraphs describe the SSPs framework and the chosen scenario.

SSPs, developed as part of the Scenario Model Intercomparison Project (ScenarioMIP) for CMIP6, offer a framework to explore the interactions between socioeconomic development and climate change. SSPs integrate with Representative Concentration Pathways (RCPs), which define greenhouse gas concentration trajectories based on radiative forcing levels. This integration enables researchers to investigate how societal factors such as economic growth, population trends, and energy use influence emissions and climate impacts (O'Neill et al. 2016, Eyring et al. 2016).

The SSP5 scenario, coupled with RCP8.5 (SSP5-8.5), represents a high-emissions pathway characterized by rapid economic growth and reliance on fossil fuels, with minimal implementation of climate policies. This scenario projects high energy consumption, increased urbanization, and significant greenhouse gas emissions, leading to a radiative forcing of 8.5 W/m^2 by 2100 (Figure 3.1) (O'Neill et al. 2016).

SSP5-8.5 highlights extreme climate outcomes, including Arctic sea ice loss. Models such as CESM2 project nearly sea ice-free summer conditions before 2050 under this scenario (DeRepentigny et al. 2020). Additionally, it forecasts widespread permafrost thaw, potentially releasing substantial amounts of carbon dioxide and methane, further amplifying climate change. Arctic warming under this pathway is projected to exceed four times the global average, illustrating the severe regional impacts of this high-emissions trajectory (Chylek et al. 2022).

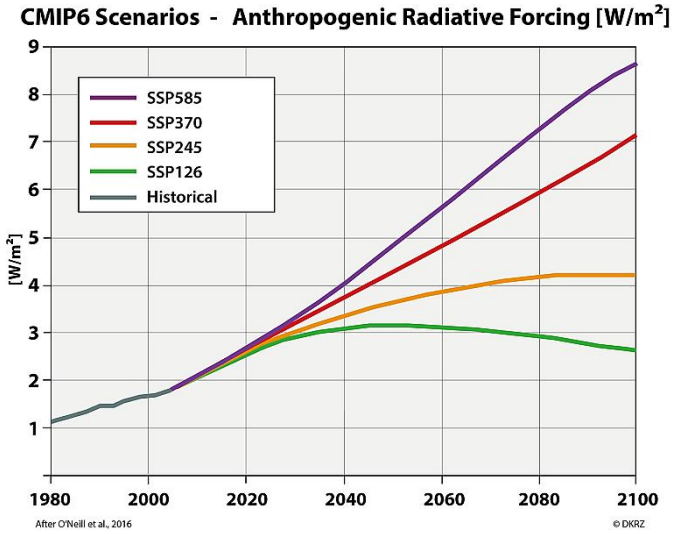


Figure 3.1: Evolution of the greenhouse-gas induced radiative forcing under different Shared Socioeconomic Pathways (SSPs) in the Coupled Model Intercomparison Project Phase 6 (CMIP6). Credit : Böttinger & Kasang (n.d.) based on O'Neill et al. (2016).

3.2 RILEs and model assessment for sea ice extent and permafrost

To identify the extreme RILE within the model, the methodology is adapted from the approach outlined by Holland et al. (2006) and further refined by Sticker (2022). This method analyzes September Arctic SIE data, retrieved using the variable "siextentn" (« Total area of all Northern-Hemisphere grid cells that are covered by at least 15% areal fraction of sea ice »[2]). A 5-year moving average is applied to reduce inter-annual variability and emphasize medium-term trends.

Variations are quantified by calculating the centered temporal derivative of the

[2] `https://clipc-services.ceda.ac.uk/dreq/u/5917b45c-9e49-11e5-803c-0d0b866b59f3.html`

smoothed series using finite differences. A RILE is defined when this derivative exceeds a threshold of three times the standard deviation of the historical dataset (1850–2014). The duration of each RILE is determined by identifying the points where the derivative intersects a horizontal line corresponding to one standard deviation. These intersection points mark the beginning and end of each event.

In the CESM2-WACCM model under the SSP585 scenario, five ensemble members are available (r1i1p1f1, r2i1p1f1, r3i1p1f1, r4i1p1f1, r5i1p1f1). Among these, only the r1 and r3 members exhibit RILEs, with the strongest event occurring in r1 (Figure 4.1). Ensemble members represent individual simulations under the same external forcings (SSP585 in this case) but with different initial conditions. This approach captures the natural internal variability of the climate system. Differences between members reflect this variability and provide a range of possible outcomes. By averaging these members, the underlying climate signals due to external forcings can be isolated from internal variability (Eyring et al. 2016).

Once the strongest RILE is selected, the model's ability to simulate permafrost and sea ice is assessed. For sea ice extent, the model's September sea ice extent data for the member exhibiting the RILE is compared to observational data from the National Snow and Ice Data Center (NSIDC 2024), covering the period 1979–2024. To compare modeled and observed data, linear regressions (1979–2024), mean bias, Mean Absolute Error (MAE), and Root Mean Square Error (RMSE) are calculated. Mean bias quantifies the average difference between predictions and observations, indicating over- or underestimation. MAE reflects the average error magnitude, while RMSE highlights larger errors. Since RMSE is optimal for normally distributed errors, a Shapiro-Wilk test is used to assess normality (Razali & Wah 2011, Hodson 2022).

For permafrost assessment, permafrost areas within the model are identified using the methodology outlined by Burke et al. (2020). This approach utilizes the Dzaa, which is suitable for models with sufficiently deep soil profiles, as the Dzaa typically reaches a depth of approximately 20 m. The Dzaa is defined as the soil depth at which annual temperature variation remains within ± 0.1°C. Permafrost presence is determined in areas where the Dzaa temperature is below 0°C. Although this method does not differentiate between continuous, discontinuous, sporadic, or isolated permafrost, it provides a binary indicator of permafrost presence.

Annual calculations are performed to generate a time-evolving permafrost mask. Once these masks are obtained for the model member associated with the RILE, a simple evaluation is performed by comparing the observed continuous and discontinuous permafrost extent from Obu et al. (2021) with the modeled presence

of permafrost. Averages for both datasets are calculated for the period 2015–2019.

3.3 Permafrost response and causes

To assess the statistical significance of the RILEs impacts, a consistent method is applied throughout the study, regardless of whether the variables pertain to permafrost or climate dynamics. This approach, inspired by Lawrence et al. (2008) and Paquin et al. (2013), has been adapted to align with this study's objectives.

Linear regression is used for trend analysis, direct comparisons of trends during and outside the RILE period are avoided unlike the methodology of Lawrence et al. (2008), as the strong RILE (2031–2043) in ensemble member r1 is preceded by a smaller RILE (2022–2027) within the same member, introducing potential bias. Instead, the linear trend during the RILE is compared to the trend of a centered climatological average (2023–2053), derived from three ensemble members without RILEs (r2, r4, r5). This approach helps isolate the RILE signal from the background climate change signal and demonstrates that the RILE-induced signal is robust.Trend differences are computed by averaging periods with similar seasonal patterns: NDJ (November–December–January), FMA (February–March–April), MJJ (May–June–July), and ASO (August–September–October).

The statistical significance of trend differences is assessed using a t-distribution test adapted for climate series trend comparisons from Zuo et al. (2019), with a p-value threshold of 0.05. This test requires a normal distribution of the linear regression residuals. Normality is tested using the Shapiro-Wilk test, which is suited for small samples (Razali & Wah 2011). The Shapiro-Wilk test results, averaged across six regions of interest (Figure 3.2) and periods (ASO, NDJ, FMA, MJJ), confirm the normality of residual distributions (not shown). Therefore, the t-distribution test from Zuo et al. (2019) is appropriate.

Permafrost response

To detect a RILE signal and assess its impact on the permafrost, relevant surface variables are selected for initial analysis. TAS ("tas") and snow depth ("snd") are identified as primary factors influencing permafrost conditions. Trends in these variables are compared to evaluate their effects on surface conditions. Snow depth data are filtered to exclude abnormal values over Arctic glaciers and the Greenland ice sheet, retaining only values below 2 meters of snow depth to avoid skewed

results.

Permafrost indicators using the soil temperature data ("tsl") are selected based on Smith et al. (2022) and categorized into shallow and deep. Evolving permafrost masks from Section 3.2 are used to extract data exclusively from simulated permafrost regions. Shallow indicators, reflecting short-term impacts influenced by seasonal variability, include ALT (maximum annual thaw depth), mean monthly ground surface temperature (MMGST) at 0.2 m depth, and surface offset (SO), calculated as the difference between MMGST and TAS. Deep indicators, representing long-term changes with minimal influence from surface variability, include ground temperature at 10 m depth (GT10m) and the Dzaa.

Annual and monthly trend difference maps are generated for the same periods as TAS and SND to ensure consistency. Complete soil temperature trend profiles, averaged for the Arctic (60°–90°N), are analyzed to track vertical and horizontal signal propagation through the soil over the year. Additionally, a curve showing permafrost area coverage by latitude is used to identify whether the signal affects regions with substantial permafrost.

Time series graphs of annual mean values for each variable from 2015 to 2100 illustrate variability over time and highlight pronounced signals during the RILE. Regional analyses focus on Alaska, Nunavut, Svalbard, the Kara Sea, and Chukotka (Figure 3.2), which exhibit distinct behaviors across locations.

Simple Pearson correlation tests between SIE and other variables for the RILE ensemble member are conducted to provide preliminary insights into mutual influences. Annual correlations from 2015 to 2100 reveal both long-term relationships and event-specific interactions. However, only 13 of 48 cases (variables and their averages across six regions) exhibit a normal distribution based on the Shapiro-Wilk test.

Causes of the permafrost response

To investigate the underlying causes of the observed permafrost signal, climatic conditions are analyzed by comparing trends as described previously. This study focuses on changes during the RILE relative to a climatological mean, without distinguishing whether all observed changes are causes or consequences of the RILE. The analysis is divided into three sections: (1) changes in surface Arctic Ocean conditions, (2) changes across different altitudes in the atmosphere, and (3) changes in surface conditions over permafrost regions.

(1) Surface Arctic Ocean conditions are directly influenced by sea ice loss. Regional and global effects of sea ice loss on surface conditions are assessed by calculating differences in sea ice concentration (SIC) between the start and end of the RILE to identify areas with significant loss. Anomalies in SEB trends are derived using Equation (1), incorporating "rls" (net downward longwave radiation at the surface, W/m^2), "rss" (net downward shortwave radiation at the surface, W/m^2), "hfss" (surface upward sensible heat flux, W/m^2), and "hfls" (surface upward latent heat flux, W/m^2). The surface is defined as the lower boundary of the atmosphere. Additionally, anomalies in sea surface temperature (SST, "tos") and TAS ("tas") trends are computed.

(2) Changes across the atmosphere are examined using variables spanning from 1000 hPa to 1 hPa, along with single-level variables. The analyzed variables include the air temperature ("ta"), meridional wind ("va", positive northward), zonal wind ("ua", positive eastward), and total cloud coverage percentage for the atmospheric column ("clt"). The northward and upward components of the Eliassen-Palm Flux ("epfy" and "epfz") are useful for assessing interactions between the troposphere and stratosphere via planetary wave activity that disrupts the polar vortex. However, these variables were not available for this study (Liang et al. 2024).

(3) Surface conditions directly affecting permafrost are analyzed using the SEB components described in section (1), with an additional term representing snowmelt energy, as detailed by Hoelzle et al. (2022). The snowmelt energy (W/m^2) is incorporated into the SEB by multiplying the surface snowmelt flux ("snm", kg/m^2s) by the latent heat of fusion (336 000 J/kg). Additional surface variables are also analyzed, including near-surface specific humidity ("huss"), precipitation ("pr", both liquid and soli), TAS, snow depth ("snd"), sea level pressure ("psl"), leaf area index ("lai"), and two soil variables: total soil liquid water content ("mrlso") and total soil frozen water content ("mrfso").

Correlation analysis between trend anomalies of these variables and MMGST anomalies identifies those most strongly associated with temperature trends at 20 cm depth. Shapiro-Wilk tests confirm non-normal distributions in 221 of 264 cases. Outliers are detected in 210 cases using the Median Absolute Deviation (MAD) method. These findings support the use of Spearman correlation, which is robust in the presence of non-normality and outliers (Zar 1972, Leys et al. 2013, Sedgwick 2014).

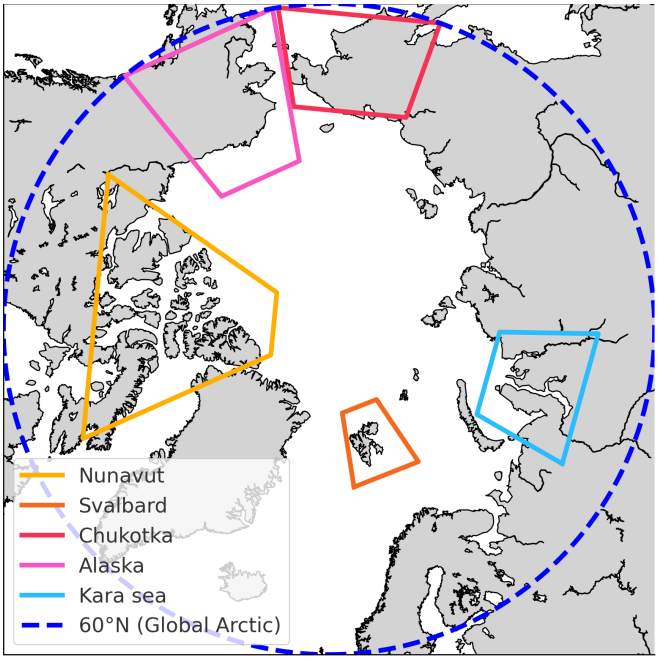


Figure 3.2: Selected regions for the analysis.

4 Results

4.1 Model verification and RILE selection

The selected RILE for this study corresponds to an extreme September sea ice loss during the period 2031–2043 (Figure 4.1) in ensemble member r1i1p1f1. During this event, SIE declines by more than 5 million km^2 over 13 years, with a reduction of approximately 4.5 million km^2 based on a 5-year rolling mean. By the end of the RILE, the Arctic Ocean becomes nearly sea ice-free in September, with SIE falling below 1 million km^2. Post-RILE, the Arctic remains sea ice-free during September, with minor increases in SIE failing to surpass the 1 million km^2 threshold and subsequently declining further.

Comparison with SIE observations from the NSIDC highlights an overestimation of SIE in the selected ensemble member with a mean bias of $0.43 \times 10^6 \text{km}^2$, a MAE of $0.64 \times 10^6 \text{km}^2$, and a RMSE of $0.79 \times 10^6 \text{km}^2$, indicating the presence of larger errors. These results suggest some limitations in the model representation of Arctic sea ice dynamics. However, for this ensemble member, the SIE is relatively close to the observations, and the linear trends of simulated and observed SIE are comparable, with $-0.070 \times 10^6 \text{km}^2\text{yr}^{-1}$ and $-0.078 \times 10^6 \text{km}^2\text{yr}^{-1}$, respectively.

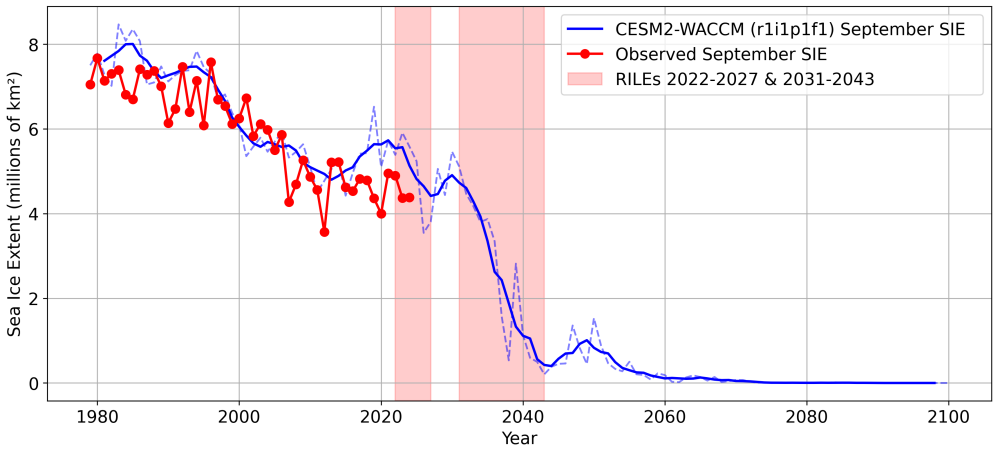


Figure 4.1: September Sea Ice Extent (SIE) in ensemble member r1i1p1f1 from CESM2-WACCM (the blue solid line is the 5 year rolling mean) compared with satellite SIE observations from NSIDC (2024).

The Dzaa method effectively identifies permafrost areas, demonstrating good agreement with observational data (Figure 4.2 and 2.2). This approach provides

a binary indicator of permafrost presence and accurately represents permafrost distribution in northern Russia, including sporadic regions (Figure 2.2). However, the model underestimates permafrost extent in Alaska and fails to capture discontinuous and sporadic regions in Scandinavia.

Despite these limitations, the method reasonably approximates overall permafrost extent. To differentiate warm and cold permafrost regions, the -2°C isotherm at the Dzaa is shown (green line), based on Burke et al. (2020). Warm permafrost, which is sensitive to temperature changes, has a limited spatial extent. Whereas the coldest permafrost occurs in Nunavut, where Dzaa temperatures reach approximately -18°C between 2015 and 2019 (Figure 4.2).

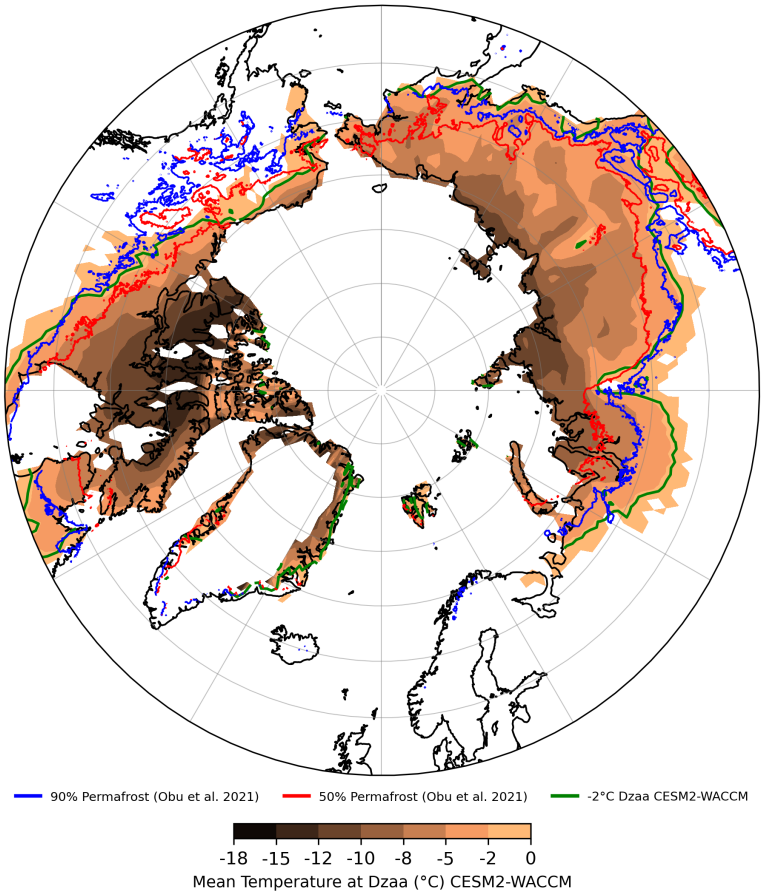


Figure 4.2: Modeled permafrost extent based on the Dzaa temperature distribution for 2015–2019 from CESM2-WACCM, showing the -2°C isotherm (green line) and areas of warm and cold permafrost. Observational data from Obu et al. (2021) representing discontinuous and continuous permafrost margins in blue and red, respectively.

4.2 Permafrost response

The analysis begins with surface conditions, focusing on TAS and SND as primary factors influencing the surface energy balance of permafrost. This is followed by an examination of shallow and deep ground signals, including the vertical and horizontal propagation of these signals. Temporal variability is assessed by comparing observed trends to the variability during 2015–2100. Finally, correlations between variables and SIE are evaluated to explore the possibility of causal interactions.

Surface air temperature and snow depth

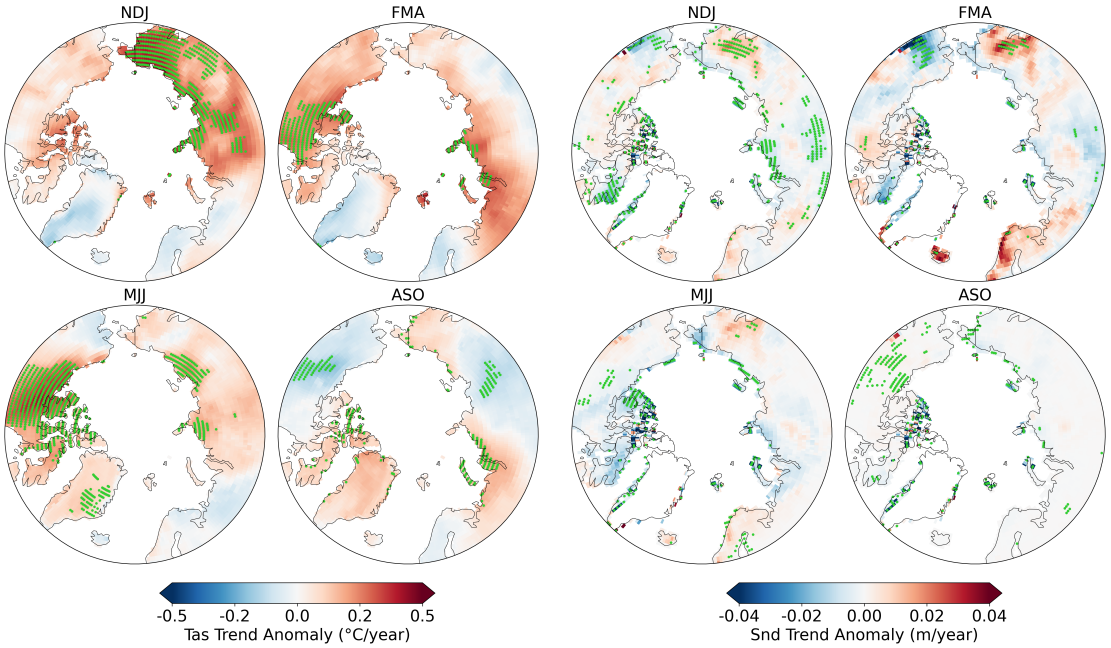
Figure 4.3a illustrates regional and seasonal variations in TAS trend anomalies across the Arctic. Northern Russia, particularly Chukotka and the coastal regions, experiences warming during early and mid-winter (NDJ), with local trends reaching up to 5°C per decade, in addition to the background climate change. From late winter through July, consistent warming is observed in Nunavut and the Kara Sea, with trend anomalies peaking during MJJ (locally approaching 5°C per decade) and FMA (approximately 3°C per decade).

In terms of ratio (Figure A.1), regions such as the Kara Sea, Alaska, and Chukotka exhibit seasonal warming rates up to four times faster than the climatological average during the RILE, while Nunavut warms at more than four times the average rate during MJJ. Across Arctic lands (60–90°N), the average ratio of warming is approximately 2.5 times faster during NDJ, FMA, and MJJ, and around 1.5 times faster during ASO.

While general warming dominates, some regions, including Greenland, Scandinavia, Iceland, Alaska, Northern Territories, and Siberia, show cooling trends seasonally. These cooling signals are typically weak, with statistical significance only in Siberia and the Northern Territories. Understanding these contrasting warming and cooling patterns requires further investigation into the underlying processes.

SND trends (Figure 4.3b) reveal localized, statistically significant anomalies during winter and early spring. Southern Chukotka (figure 3.2), including adjacent areas, experiences the most notable increase in SND, reaching approximately 40 cm per decade. Conversely, Alaska shows decreases of similar magnitude, creating a dipole pattern around the Bering Strait. These localized anomalies are masked when analyzing spatial averages. Nunavut and Baffin Island show sporadic, weak

positive SND anomalies throughout the year. Persistent anomalies appear along the margins of glaciers and ice sheets in Greenland, Svalbard, and Nunavut, likely stemming from model limitations in simulating snow depth near ice masses.



(a) TAS

(b) SND

Figure 4.3: Seasonal near-surface (2m) air temperature (TAS) and snow depth (SND) trend anomalies during the RILE 2031-2043 of the r1i1p1f1 ensemble member of CESM2-WACCM. Green dots are the significant anomalies using a t-test and a p-value threshold of 0.05. The trend anomaly is the difference of the linear trend during the RILE 2031-2043 and the trend of a centered climatological mean 2023-2053 of three RILE free ensemble members (r2i1p1f1, r4i1p1f1 and r5i1p1f1).

Shallow ground

Whether in the soil or for TAS, the signal is constant near the ocean but does not propagate uniformly inland (Figure 4.3a and 4.4). This pattern suggests the involvement of mechanisms beyond the straightforward warming of land adjacent to regions that have experienced sea ice loss.

An analysis of subsurface temperature trends at a depth of 20 cm, derived from MMGST, reveals that nearly all permafrost regions except for the southern part of the Russian permafrost exhibit a warming signal that is both more spatially extensive and statistically significant compared to TAS anomalies (Figure 4.4).

This finding highlights the internal variability of TAS and the thermal inertia of the ground, along with other processes contributing to subsurface warming during the RILE.

A warming signal emerges during the NDJ season in regions such as Chukotka, Nunavut, areas surrounding the Kara Sea, Svalbard, and Greenland. This signal at 20 cm depth peaks during NDJ and FMA, with average warming trends reaching up to 4°C per decade in highly responsive regions. In contrast, TAS anomalies in these regions neither achieve comparable magnitudes nor statistical significance, suggesting that the observed warming is likely amplified by additional heat sources beyond TAS. As winter fades away, the warming signal pattern persists with reduced intensity; weak yet significant warming continues in Nunavut and the Kara Sea.

MMGST anomaly ratios averaged over the regions (Figure A.1) show that Svalbard and Alaska, represented by fewer grid cells, exhibit the highest ratios, with warming up to 12 times faster during the RILE for Alaska in late winter. However, this warming is not statistically significant, and their anomalies in °C are lower than those in other regions. On average, Arctic permafrost (60–90°N) exhibits statistically significant warming up to three times faster at a depth of 20 cm during NDJ, FMA and MJJ. Regions such as Nunavut, Chukotka, and the Kara Sea display similar magnitudes of warming ratios but in different seasons.

ALT trends exhibit the most pronounced changes at the permafrost margins, particularly in areas classified as "warm" permafrost (Figure 4.5). Along the North American permafrost margins, ALT displays a decreasing trend, albeit over a limited area. Conversely, Eurasian regions display ALT increases, with localized trends exceeding 4 m per decade.

To interpret SO trend anomalies (Figure 4.4), it is essential to consider average values across both the RILE ensemble member and the climatological mean, which demonstrate a seasonal dependence. During NDJ and FMA, SO is negative, indicating lower surface air temperatures relative to ground temperatures. In MJJ, SO becomes positive, meaning higher surface air temperatures relative to the ground. During ASO, SO exhibits a mix of positive and negative values (not shown). A negative SO trend anomaly in NDJ and FMA therefore suggests an increasing temperature gradient between the air and ground, likely due to enhanced surface insulation. In contrast, a positive trend during these periods implies reduced insulation.

During winter and early spring, regions with increasing snow thickness exhibit

higher insulation, while areas with decreasing snow thickness display lower insulation (Figure 4.4). Chukotka exhibits a decrease in SO, coinciding with areas of higher snow accumulation, peaking at an increase of up to 4°C per decade during FMA. In contrast, localized areas in Russia show SO increases during NDJ. Similarly, Nunavut experiences SO decreases in areas with minor snow accumulation. Around the Kara Sea, SO increases are observed but are not directly linked to changes in snow thickness. Regions experiencing SO increases during winter correspond to areas of pronounced warming, suggesting that cold winter air is increasingly unable to penetrate the ground and cool permafrost. However, SO changes during MJJ and ASO are weaker and more complex to interpret.

Deep ground

With increasing depth, the temperature signal diminishes in magnitude; however, the extent of the statistically significant signal expands and persists throughout the year. It highlights the influence of long-term forcing mechanisms, such as the 13 years of extreme sea ice loss (Figure 4.4). The signal also exhibits a temporal lag relative to surface changes, requiring time to propagate to a depth of 10 meters.

The strongest signals occur during the MJJ and ASO seasons, with trends up to 2°C per decade locally. On average, the warming ratio oscillates around 2 times faster throughout the year with values for Alaska more than 5 times faster during ASO and Svalbard almost 5 times faster as seen for MMGST (Figure A.1).

For Dzaa, unlike ALT, the most affected areas correspond to regions with the cold ice-rich permafrost (Figure 4.2), particularly in Nunavut and the Kara Sea regions (Figure 4.5). Along the permafrost margin in North America, where ALT exhibits a decreasing trend, Dzaa also shows a decrease. Regardless of whether the trend indicates a decrease or increase, simulated values typically range between ±20 m per decade.

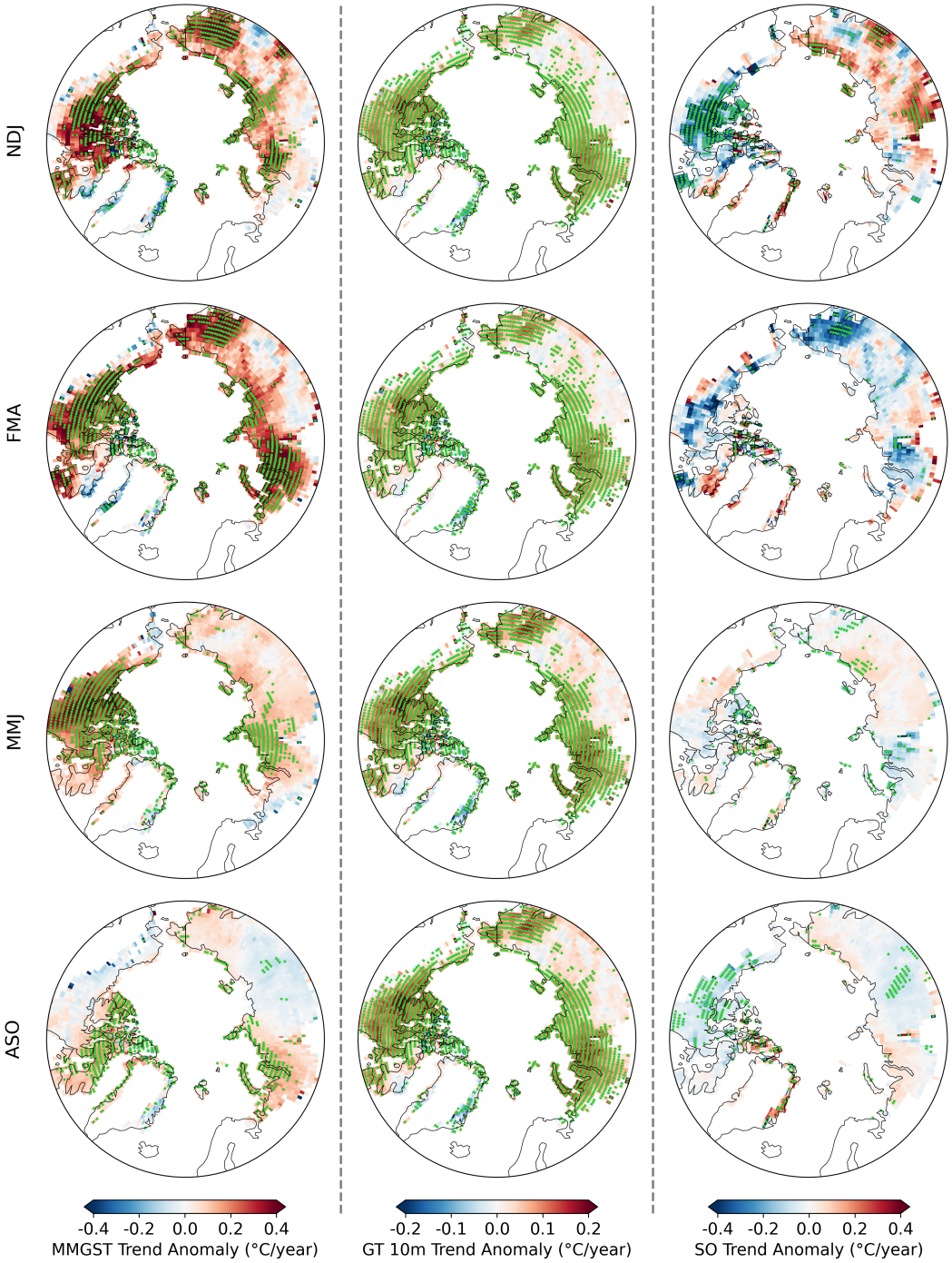


Figure 4.4: Seasonal permafrost trend anomalies of MMGST (Mean Monthly Ground Temperature at 20cm depth), GT10m (Ground Temperature at 10m) and SO (Surface Offset) during the RILE 2031-2043 from CESM2-WACCM r1i1p1f1. Green dots are the significant anomalies using a t-test and a p-value threshold of 0.05.

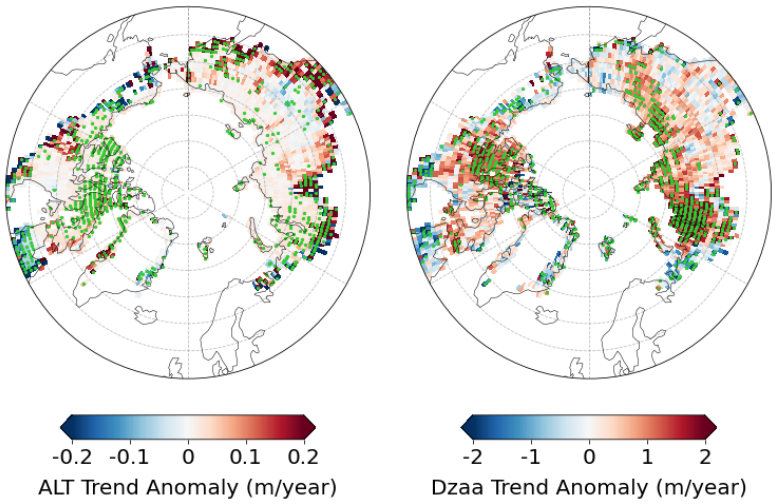


Figure 4.5: Annual permafrost trend anomalies of ALT (Active Layer Thickness, maximun annual thaw depth) and Dzaa (Depth of zero annual amplitude) during the RILE 2031-2043 from CESM2-WACCM r1i1p1f1. Green dots are the significant anomalies using a t-test and a p-value threshold of 0.05.

Vertical and horizontal propagation of the signal

When averaged across longitudes (Figure 4.6), the permafrost temperature profile reveals a statistically significant warming signal at nearly all depths (not shown), except seasonally in the uppermost centimeters of more southern regions. In these areas, higher variability reduces the significance of the signal, likely due to the increased distance from the Arctic Ocean.

The warming signal first appears at the surface in November in regions adjacent to the Arctic Ocean. As winter progresses, the signal intensifies, reaching a peak of approximately 3°C per decade by January. During this time, the warming propagates downward into the permafrost and southward toward lower latitudes. From February onward, the signal continues its downward and southward progression, reaching latitudes of 55°–60°N and depths of 10–15 meters. However, as the signal penetrates further south and deeper into the permafrost, its intensity gradually weakens. The strongest warming signals are concentrated in areas with extensive permafrost, highlighting their particular sensitivity to climate-driven changes.

During the summer months of July and August, a distinct warming signal emerges at the surface, with an average magnitude of approximately 1°C per decade. Unlike the winter signal, this summer warming does not penetrate below

the first meter of soil. In September and October, no new surface warming signal is simulated. However, remnants of the previous winter's warming signal persist in deeper layers. This persistence underscores the long-term thermal inertia of permafrost and the gradual nature of heat transfer in subsurface layers.

At latitudes above 80°N, both cooling and warming trends are simulated. However, these high latitudes encompass relatively small permafrost areas with limited data. Isolated anomalies, such as those in northern Greenland, influence regional averages, complicating the generalization of findings.

When specific regions of interest are analyzed separately (Figure 4.7), regional processes influence arises. For instance, while Nunavut does not exhibit the strongest average TAS signal, it contains localized areas with some of the most intense warming signals. Nunavut displays a consistent warming signal across all depths, but its temporal evolution is discontinuous. The lands surrounding the Kara Sea display the strongest and deepest warming signals. In the upper few meters of soil, the warming trend exceeds 4°C per decade. However, the onset of this warming occurs later than the Arctic average, beginning between December and January. Similar to the Chukotka region, a secondary surface warming signal emerges during July and August.

In summary, while a general pattern of warming propagation is apparent across the Arctic, regional differences in the intensity, timing, and depth of warming signals are notable. These variations underscore the complex and heterogeneous nature of permafrost responses to Arctic warming, emphasizing the importance of localized analyses in understanding these dynamics.

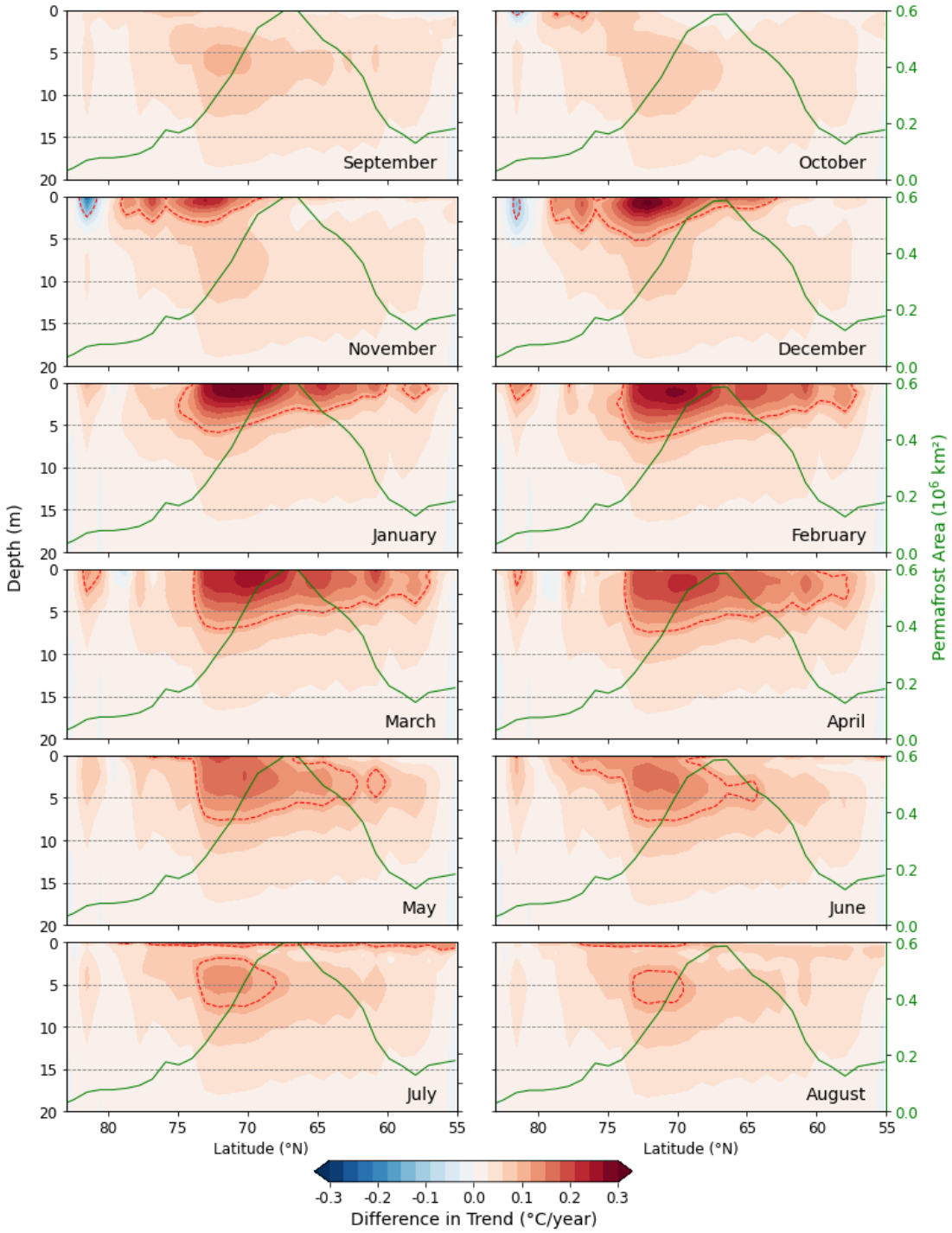


Figure 4.6: Arctic permafrost monthly trend anomalies of ground temperatures during the RILE 2031-2043 from CESM2-WACCM r1i1p1f1. The green line is the total area of permafrost for each latitudes and the dashed red line is the +/- 1°C trend anomaly isotherm.

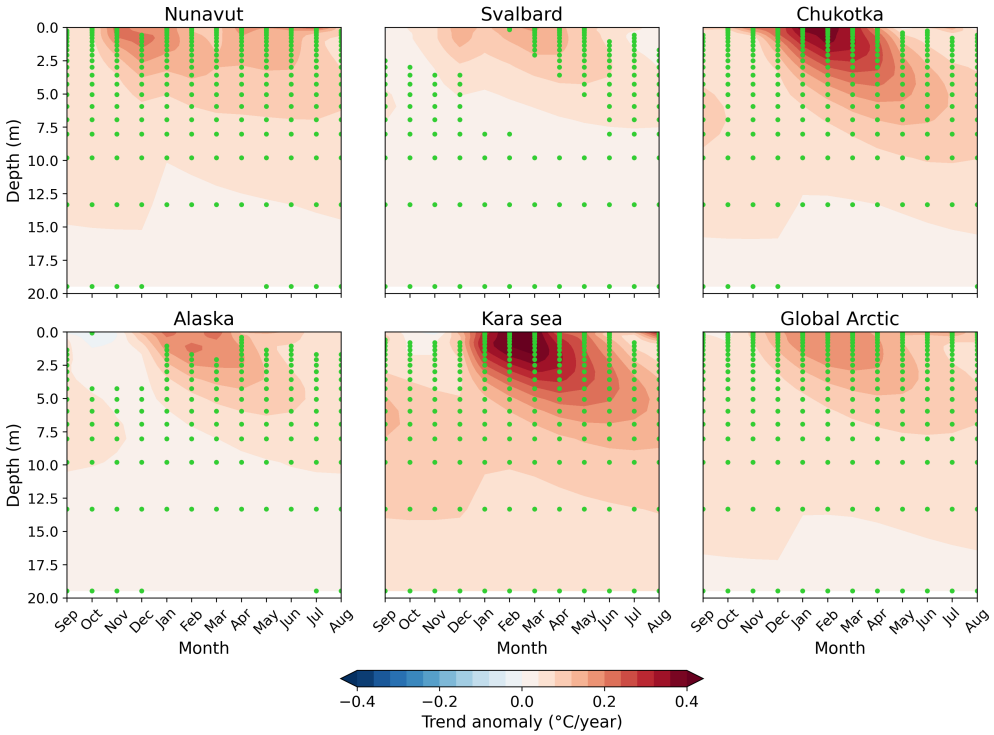


Figure 4.7: Regional permafrost monthly trend anomalies of ground temperatures during the RILE 2031-2043 from CESM2-WACCM r1i1p1f1. Green dots are the significant anomalies using a t-test and a p-value threshold of 0.05. Refer to figure 3.2 for region definitions.

Permafrost response overview and general variability

Even in annual averages (Figure 4.8), where stronger seasonal anomalies are partially masked by weaker summer trends, the signal remains evident for certain variables, though not all of them. The exact trend values during the RILE 2031-2043 and the statistical significance of the difference with the climatological trend average can be found in the appendix (Table A.1). Variables measured at greater depths are more likely to exhibit statistically significant trends due to reduced short-term variability.

One variable not yet analyzed is the permafrost extent (PE), as shown in Figure 4.8. The PE exhibits a decline toward the end of the RILE period. This decline is expected to be delayed, as permafrost extent is determined based on the Dzaa. Several years of warming are required for the thermal signal to propagate to the Dzaa, raising its temperature above 0°C or leading to its complete disappearance. Moreover, even if the soil temperature remains below 0°C, the classification method

excludes areas from being defined as permafrost if the entire temperature profile fluctuates by more than 0.1°C throughout the year.

The most pronounced decline in PE is simulated across the Arctic as a whole, particularly in Nunavut. The data suggest that the previous RILE period (2022–2027) was neither sufficiently long nor intense to exert a substantial influence on PE. However, once the Arctic Ocean becomes sea ice-free in September, whether in the primary RILE member or the three additional RILE scenarios PE becomes unstable. It begins to oscillate and decline, eventually disappearing entirely by 2100. A similarly delayed response is observed in deeper ground layers. Warming signals at these depths emerge several years after the onset of the RILE, but they are more consistent and interpretable due to reduced variability compared to shallower or surface variables.

The behavior of the Dzaa from 2015 to 2100 is notably complex. Initially, the Dzaa increases, reflecting the thawing of deeper permafrost layers. By approximately 2080, the Dzaa begins to decrease, likely due to the diminishing extent of permafrost, which by then predominantly consists of cold permafrost with a shallow Dzaa. Following this phase, the Dzaa increases again as the remaining cold permafrost continues to warm.

This analysis underscores the varying sensitivity of surface and subsurface permafrost dynamics to external climatic forcing. The findings highlight the importance of considering both spatial and temporal scales to interpret permafrost responses under changing climatic conditions.

Correlation with the sea ice extent

As shown in Figure 4.9, the strongest correlations between SIE and other variables occur during the RILE period compared to other years between 2015 and 2100. Exceptions to this pattern include SND and SO, which exhibit localized variability that is not fully captured in regional or Arctic-wide averages. Whether SIE directly influences these variables, or whether they are primarily governed by atmospheric and oceanic anomalies driving the RILE or a combination of both remains an open question requiring further investigation.

For individual regions, correlations have been calculated against total Arctic SIE. However, it is likely that using regional SIE data would produce stronger and more statistically significant correlations, providing a more precise understanding of the interactions between SIE and permafrost related variables.

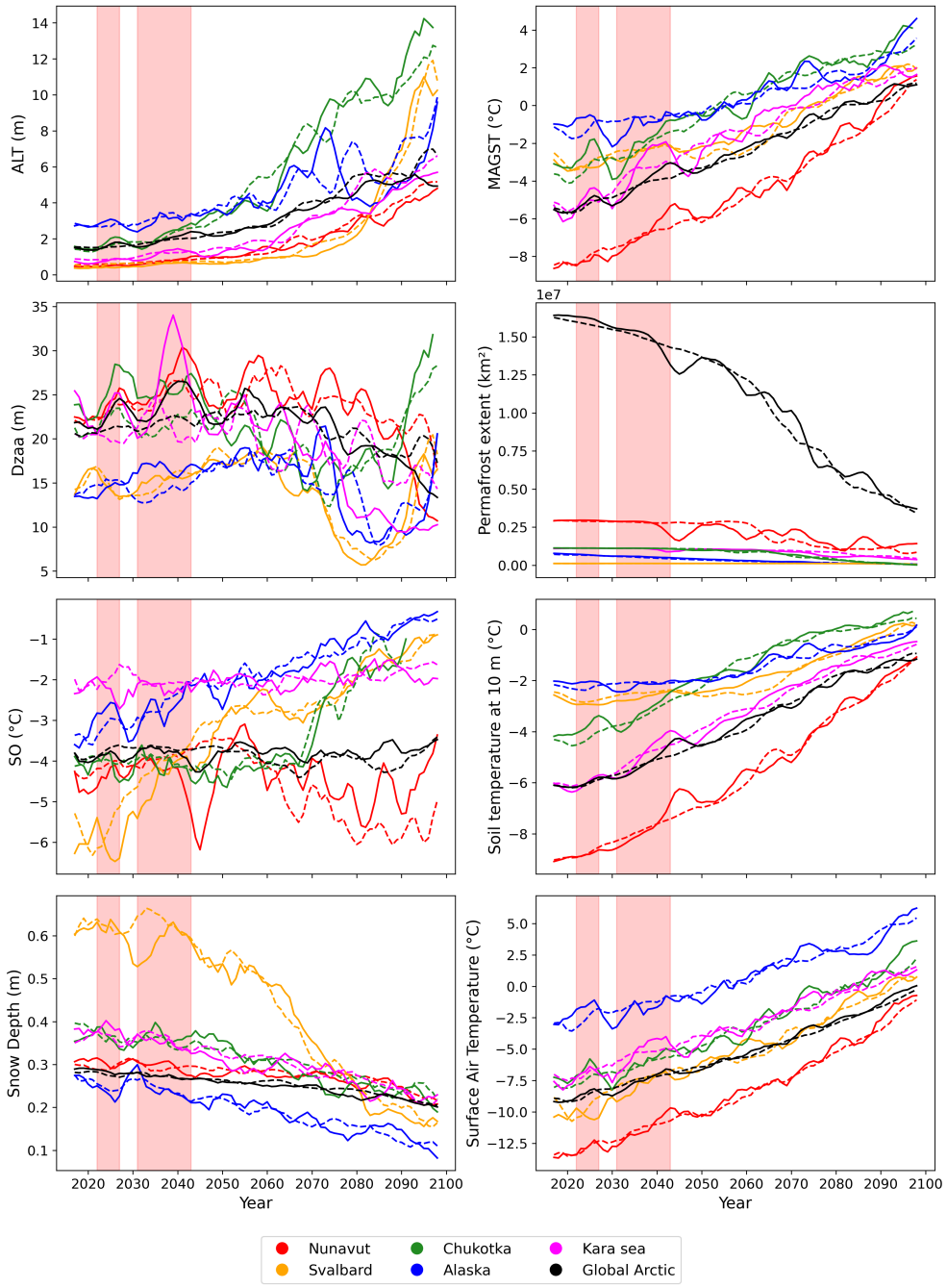


Figure 4.8: Arctic and regional annual average time series of ALT (Active Layer Thickness, maximum annual thaw depth), Dzaa (Depth of zero annual amplitude), SO (Surface Offset), snow depth, surface air temperature, ground temperature at 10m, permafrost extent and MAGST (Mean Annual Ground Surface Temperature at 0.2m) from CESM2-WACCM r1i1p1f1 (solid line) and average of r2i1p1f1/r4i1p1f1/r5i1p1f1 (dashed line). Red boxes are RILE periods r1i1p1f1 (2022-2027 and 2031-2043). Refer to figure 3.2 for region definitions. The exact trend values during the RILE 2031-2043 and the significance of the difference with the climatological trend average can be found in the appendix (Table A.1).

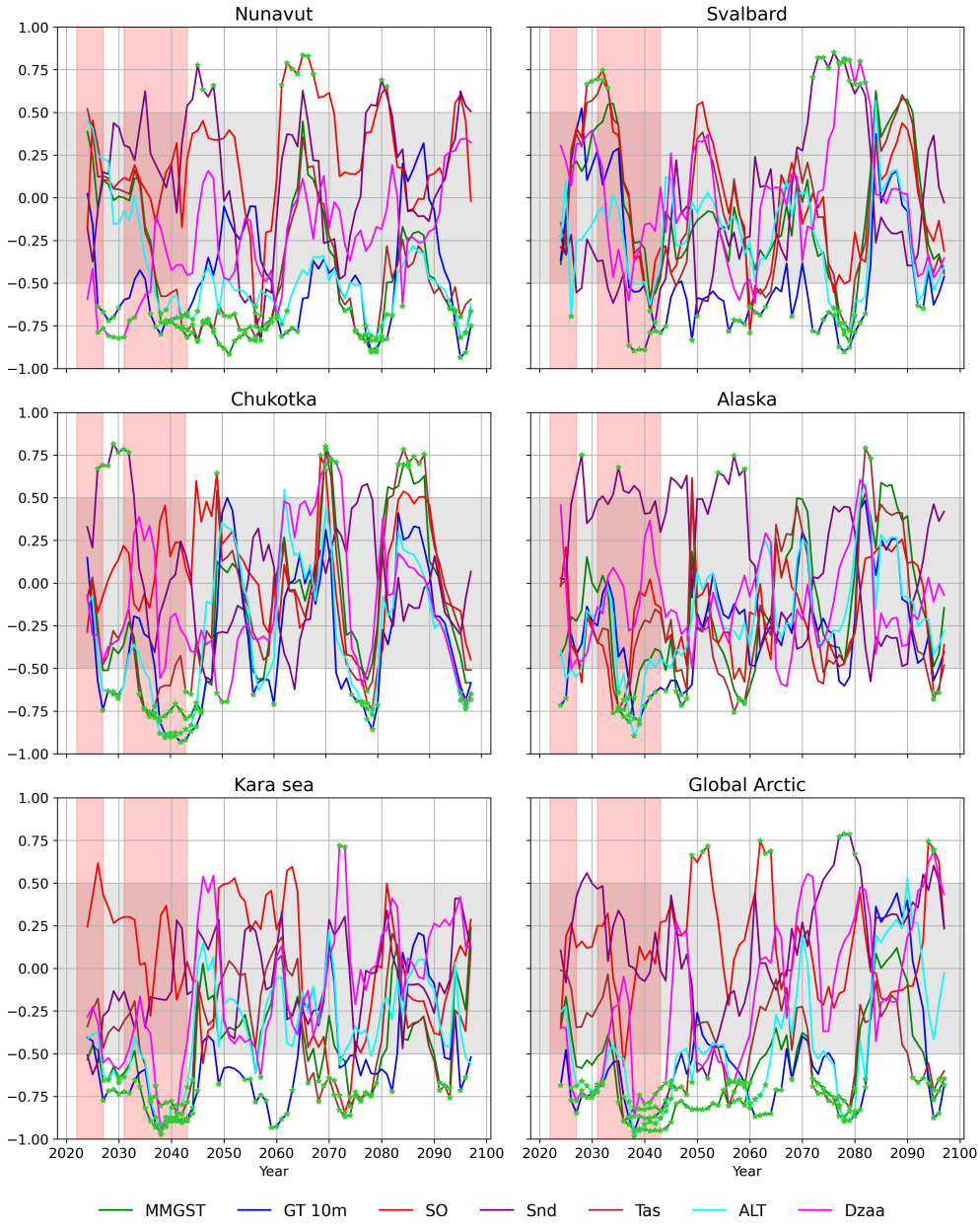


Figure 4.9: Arctic and regional annual average correlation between September SIE (Sea Ice Extent) and ALT (Active Layer Thickness, maximum annual thaw depth), Dzaa (Depth of zero annual amplitude), SO (Surface Offset), Snd (snow depth), Tas (surface air temperature), GT 10m (ground temperature at 10m), permafrost extent and MMGST (Mean Annual Ground Surface Temperature at 0.2m) from CESM2-WACCM r1i1p1f1. Red boxes are RILE periods r1i1p1f1 (2022-2027 and 2031-2043). Green dots are significant (p-value < 0.05) Pearson correlations. The y axis unit is the Pearson correlation coefficient, -1 means perfectly negatively correlated and +1, perfectly positively correlated. Refer to figure 3.2 for region definitions.

4.3 Drivers of the permafrost response

This section explores the drivers of the simulated permafrost response and the variability in its intensity and timing across different regions. The analysis incorporates sea ice loss maps (Figure 4.10), a diagram summarizing key interactions (Figure 6.1) as well as a series of maps and plots in the appendix.

It is structured into two main categories: (1) changes across the atmosphere and (2) surface processes over the ocean and land. This division allows for a detailed examination of the direct and indirect mechanisms influencing permafrost dynamics. Followed by (3) a regional analysis.

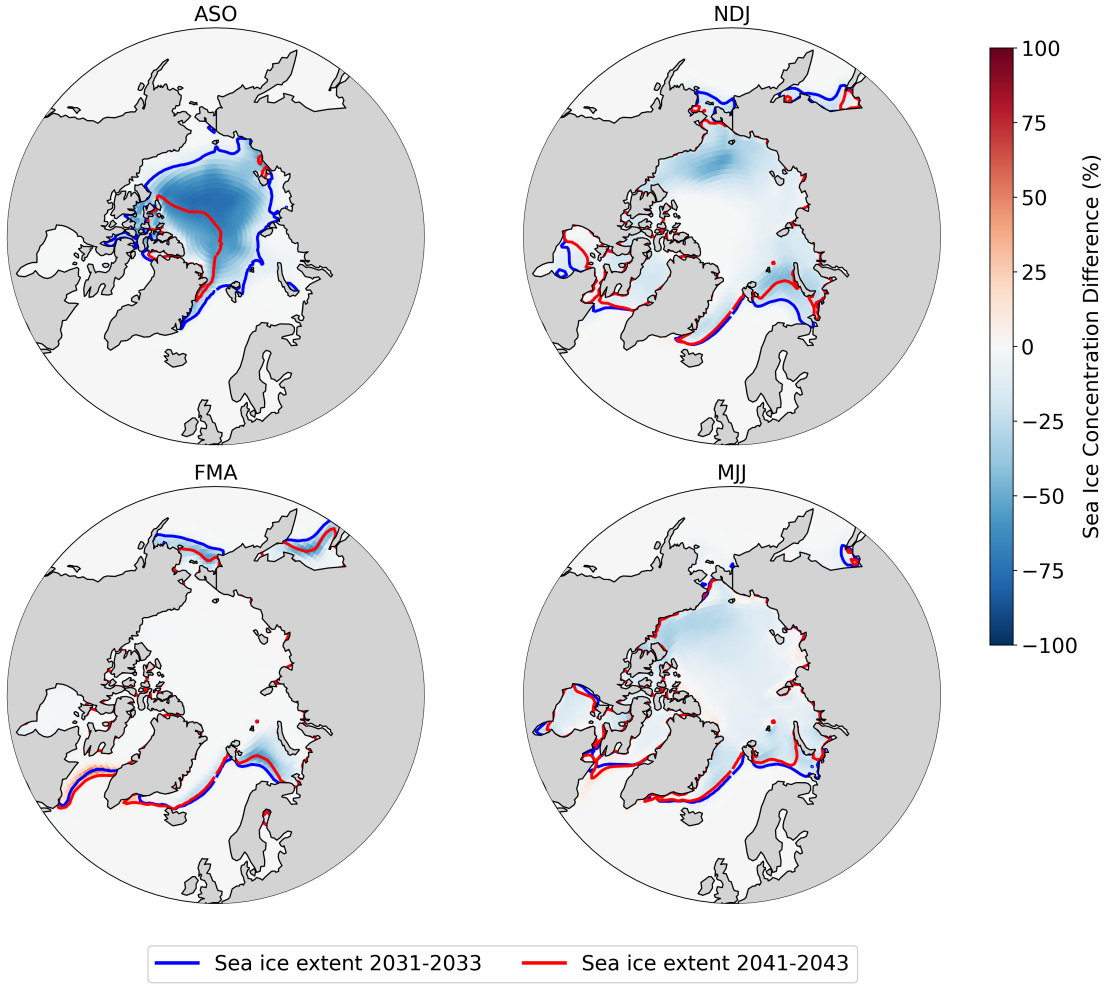


Figure 4.10: Seasonal sea ice concentration difference between the start and the end of the RILE 2031-2043 from CESM2-WACCM r1i1p1f1.

(1) Changes in atmospheric dynamics are present during the study period. The stratosphere undergoes a cooling in December, followed by a warming trend from February to April (Figure A.7). These temperature variations strengthen the polar vortex (PV) in early winter and then lead to its weakening in late winter (Figure A.6). This weakening coincides with increased jet stream oscillations in FMA, enhancing the transport of warmer air to the Arctic and colder air to lower latitudes (Figure A.5).

The extent into higher altitudes of the surface temperatures warming signal is not consistent throughout the year and the regions (Figure A.7). The surface warming signal is present early in the winter season but does not extend beyond 500–850 hPa. However, by March the signal propagates upward towards the stratosphere, leading to higher temperatures in the upper atmosphere. In late winter and early spring, this signal descends to the surface.

SLP trend anomalies are maximum around 0.5 Pascal per decade and exhibit only few statistically significant anomalies (Figure A.5). Although weak, these anomalies suggest potential shifts in oscillations and pressure patterns that govern the Arctic climate, including the ADA, NAO (North Atlantic Oscillation) and the Siberian High. These changes display strong seasonality and potential influence on winds and warmer/colder air advection toward specific regions. For instance (Figure A.5), the ADA shifts toward a negative phase in spring, intensifying Arctic winds directed toward Siberia and resulting in a cold anomaly over this region. The NAO exhibits a positive like phase during early winter, corresponding with a strong PV, and transitions to a negative like phase during ASO (Figure A.5). This shift drives zonal wind and precipitation changes over Scandinavia, particularly along the Norwegian coast (Figure A.5 and A.4).

(2) Changes in ocean surface conditions and SIC during the RILE are contributors to climatic changes (Figure 4.10). As expected, SIC is most affected during ASO, consistent with the definition of the RILE, which is based on the September SIE. By the end of the RILE, regions with SIC above 15% are constrained to areas north of Nunavut and Greenland, particularly in the Lincoln Sea. This highlights the significant reduction in SIE, leaving vast sea ice-free ocean regions. Conversely, in the Labrador Sea (south of Greenland and Baffin Island), SIE increases during late winter and spring. Outside the ASO season, other seasons exhibit less pronounced SIE retreats. The regions most affected by SIC and SIE changes include the Barents Sea, the Chukchi Sea, and the Okhotsk Sea.

SST anomalies (Figure A.3) in the central Arctic peak during ASO, mainly driven by increased absorption of SW radiation in sea ice-free areas that become

exposed earlier in the summer. There is a lag between the strongest SST anomalies and the significant increase in SEB due to SW (Figures A.2 and A.4). These positive SST anomalies persist into winter but progressively weakens as the ocean releases excess heat, mainly through LH and SH fluxes linked with an increase in TAS (about 5°C per decade) above the ocean, especially during NDJ (Figures A.2 and A.5). These fluxes are most intense in regions where sea ice does not reform during winter (Figure 4.10) or where thin ice allows continuous heat exchanges between the ocean and the atmosphere. This warmer air above the ocean in winter impacts adjacent lands and is combined with colder/warmer air advection due to meridional wind and PSL anomalies (Figure A.5). This explains the strong warming signals in some regions and their absence in others, even in proximity to areas of great sea ice loss.

Cloud cover anomalies can add clues for SEB analysis (Figure A.4). For instance, despite negative SEB and TAS trend anomalies over central Siberia during ASO, the cloud cover exhibits an increasing trend, likely due to an increase of high cold clouds blocking SW radiation while having minimal impact on LW emissions. While an increase in cloud cover over the Arctic Ocean during NDJ is linked with the strongest TAS anomalies over the same region at that time.

The correlation between the SEB over land and the MMGST anomalies (Figure 4.11) indicates that the MJJ and ASO seasons generally display a direct correlation between SEB and MMGST anomalies. In contrast, in winter, the simple SEB computed in this study cannot account for the soil temperature trend anomalies simulated at 20 cm depth. However, other variables not included in the SEB calculation show trend anomalies directly correlated with MMGST changes. These include snow depth, precipitation, and subsurface changes, such as variations in soil frozen and liquid water content, which are indicative of freeze-thaw processes within the permafrost.

A decreasing trend of the Dzaa at the permafrost margin suggest that the increase in soil liquid water content (Figure A.3) acts as a buffer to limit the deep propagation of the warming signal. Additionally, changes in vegetation at the permafrost margin in North America, such as an increased LAI (Figure A.3, modify surface properties and seem to influence ALT and Dzaa trends.

(3) While regions such as Svalbard and the Greenland coast are affected, the focus is on three regions with the most pronounced and extensive signals: Nunavut, the Kara Sea region, and Chukotka.

Nunavut:

The colder PV in early winter appears to be associated with surface cold anomalies over the Canadian Arctic, while a warmer PV later in the season corresponds to surface warm anomalies in the same region (Figures A.7 and A.5). Both cases exhibit meridional wind anomalies at 200 hPa, suggesting potential colder or warmer air advection (Figure A.5).

During ASO, ice loss is concentrated around the Nunavut islands, whereas in NDJ–MJJ, it primarily occurs in Hudson Bay, Baffin Bay, and along the coast of the Northwest Territories. By FMA, ice loss in these regions becomes minimal. The reduction in sea ice during summer, autumn, and early winter near Nunavut increases LH and SH fluxes during winter.

Positive soil temperature anomalies in spring and summer correlate with meridional wind anomalies at 200 hPa, increased downward LW radiation due to the presence of warmer air masses, and increased SW absorption caused by a reduced cloud cover (Figures A.5,A.4, andA.2).

The correlation results (Figure 4.11) indicate that MMGST anomalies are positively correlated with the SEB during MJJ–ASO but negatively correlated during NDJ–FMA. A strong correlation between near-surface specific humidity and MMGST during MJJ aligns with increased LW absorption and LH fluxes toward the atmosphere. During winter, when the SEB is negatively correlated, snow depth exhibits the most positive correlation with MMGST, highlighting its dominant role on winter MMGST anomalies.

Kara Sea Region:

The Kara Sea, and particularly the Barents Sea, experience ice loss throughout the year. At the onset of winter, the warmer air mass forming above the ocean is not yet pronounced over the Kara Sea, likely due to meridional and zonal wind anomalies. These circulation anomalies shift in FMA, resulting in a combination of warmer air from the ocean and lower latitudes associated with meridional wind anomalies (Figures A.5).

During ASO, the region displays a warming directly linked with increased SW absorption and reduced cloud cover. While MMGST in this region exhibits a year-round increase, the variables selected for the correlation analysis do not strongly correlate with MMGST anomalies (Figure 4.11). However, a positive correlation between MMGST and soil frozen water content is observed, which contrasts with other regions.

Chukotka:

The highest increase in snow depth is simulated in the southern areas, with correlations (up to 0.8 during NDJ) between snow depth and MMGST warming (Figure 4.11). This snow depth increases is driven by higher snow precipitation in early winter and reduced snow melt in spring (Figure A.4). The absence of TAS anomalies in spring helps preserve the snowpack, even without additional precipitation. The increasing snow depth likely mitigates soil cooling during cold winter months.

During ASO, positive TAS anomalies appear to result from meridional wind anomalies, a pronounced positive PSL anomaly over the Bering Strait, and warmer air masses originating from the ocean. The causes of the strong TAS anomaly in NDJ remain less clear. The correlation between MMGST anomalies and SEB anomalies is close to zero during all the seasons except MJJ. Similar to the global Arctic and Nunavut, winter correlations in Chukotka are dominated by snow depth (SND) and total soil liquid water content (mrlso) (Figure 4.11).

To provide a concise overview while avoiding repetition, Figure 6.1 summarizes the potential causes of the permafrost response. Detailed explanations are presented in the conclusion section rather than in this section.

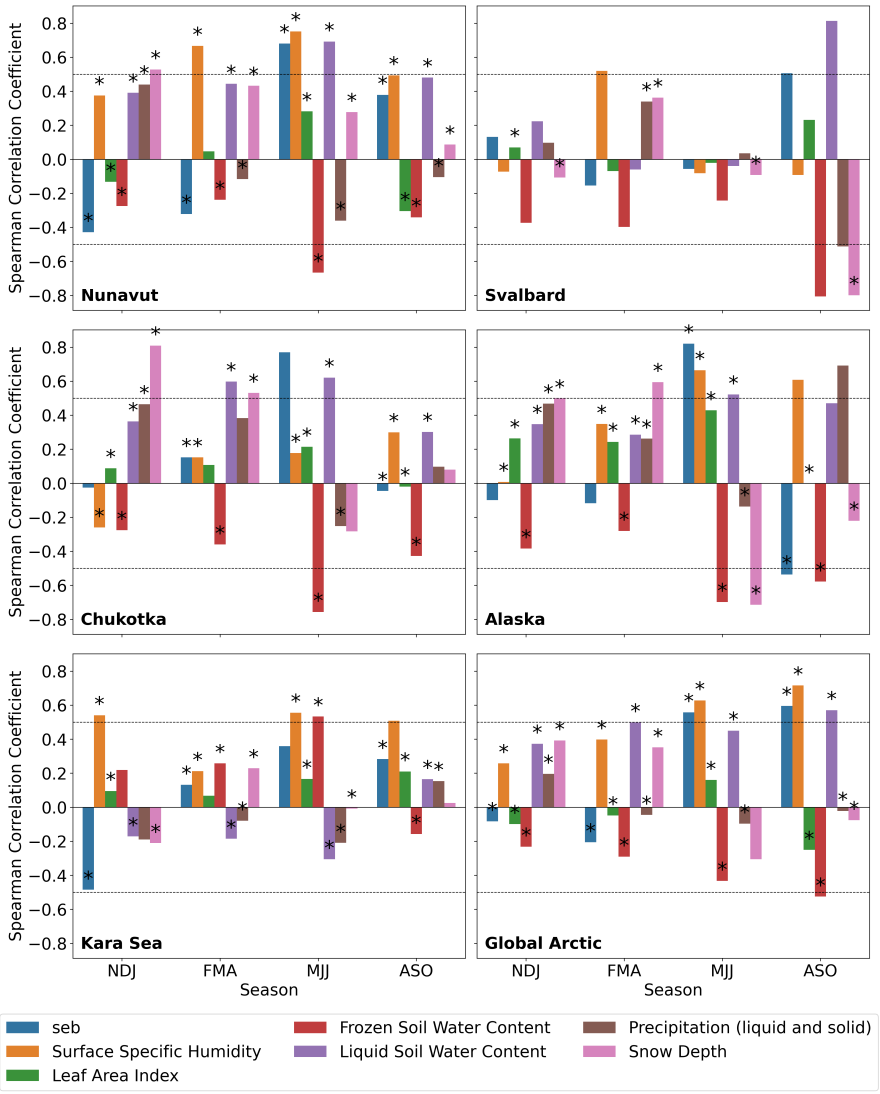


Figure 4.11: Spearman correlation coefficient and significance (black stars, p-value threshold = 0.05) between permafrost soil temperature trend anomalies at a depth of 20 cm and trend anomalies of other variables. The variable SEB represents the surface energy balance. Trend anomalies are calculated as the difference between the trends during the RILE period (2031–2043) and the trends during the centered climatological mean period (2023–2053) in the CESM2-WACCM climate model

5 Discussion

This study examines the impacts of RILEs on permafrost using a new climate model from the CMIP6 project and builds on the approach of Lawrence et al. (2008). It addresses the initial research question regarding permafrost response and the primary mechanisms involved, especially the snow depth changes. Previous studies anticipated a warming signal on land adjacent to regions experiencing sea ice loss, with more or less uniform propagation inland. However, our results reveal the influence of additional mechanisms that disrupt this uniform propagation. In some cases, areas near regions of substantial sea ice loss do not exhibit the expected warming signal and in other cases the signal is present further inland than expected.

Limitations of the study

In Alaska, limitations in the method used prevent accurate representation of the permafrost extent, despite the region showing interesting climatic changes during the RILE. Addressing this issue could be valuable for future research. In Greenland and Svalbard, interpretation is more challenging due to model resolution constraints and general snow cover anomalies near ice sheets and glaciers. A more detailed study of Svalbard would be valuable, as this region is experiencing the fastest warming on the planet Adakudlu et al. (2019), Rantanen et al. (2022).

The computed SEB is positively correlated with MMGST anomalies during summer but shows no correlations or even negative correlations during winter. The strong correlation between MMGST anomalies and SND anomalies indicates that a more advanced SEB model is required, incorporating heat transfer through the snowpack and its insulating effect on the ground. Specifically, the SEB should be calculated between the ground surface and the bottom of the snowpack. This adjustment aligns with the observed behavior in summer, when snow diminishes or disappears, and the SEB correlates well with MMGST anomalies. Additionally, significant changes in liquid and solid soil water content highlight the need for energy balance analysis within the permafrost, accounting for phase changes of water and their influence on thermal properties.

Regarding the Spearman correlation analysis, it may be more effective to evaluate the influence of variables on the permafrost response using a Geographically Weighted Regression (GWR) for instance. This approach accounts for spatial autocorrelation, which is visually evident when examining the maps. Such a method would allow for a more localized and spatially explicit understanding of

how different variables contribute to permafrost dynamics.

Short-term events, such as sudden stratospheric warming (SSW), rain on snow events, or ice-free days, are not fully captured due to seasonal averaging in this study. Future research should focus on such abrupt, short-term events and their impacts, as highlighted by Heuzé & Jahn (2024) study, which predicts the first ice-free day in the Arctic by 2030 using CMIP6 models.

Our results should be interpreted cautiously, as they are based on a single model, a single RILE, and a high-emission scenario. Future studies should incorporate multiple RILEs, models, and scenarios to validate whether similar mechanisms are at play and identify consistent regions of impact. Questions remain regarding the attribution of observed changes to determine whether they are causes or consequences of the RILE. Future studies should examine the potential irreversibility of observed permafrost changes, how far RILE events could advance permafrost thaw compared to global climate change expectations, and the minimum intensity and duration of RILEs required to affect permafrost in depth.

Comparison with other studies

Compared to Lawrence et al. (2008) study, this master's thesis shows slightly higher TAS warming, though the magnitude remains around 5°C per decade in the warmest regions. However, regional differences emerge, particularly in the timing and intensity of warming and the subsurface response simulated. This difference in TAS anomalies is attributed to warmer air advection and increase in SW absorption by the ground during summer.

In terms of atmospheric circulation, results align with prior studies (Liang et al. 2024, Chripko et al. 2021) in identifying similar patterns. However, contrary to expectations based on Liang et al. (2024) using the same climate model, the stratosphere-troposphere interactions simulated during the RILE were weaker than anticipated. Instead, it looks like conditions during smaller sea ice loss events, suggesting a potential influence of oceanic background states such as discussed in the paper.

Despite improvements in snow insulation modeling in CESM2 compared to previous models (Lawrence et al. 2019), the thick snow layers insulation effect is poorly simulated relative to other CMIP6 models (Burke et al. 2020). However, CESM2-WACCM improves representation of sea ice compared to CESM2 (DeRepentigny et al. 2020). Biases remain in the model's feedback simulations,

particularly during winter, propagating to soil anomalies. A more in-depth evaluation of CESM2-WACCM and RILE ensemble members is necessary to address biases in feedbacks and Arctic Amplification (Burke et al. 2020).

These new climate models are complex, but they are still a simplification of the great complexity in the real-world systems, particularly when considering regional characteristics and specific permafrost processes. For instance, thermokarst features such as lake formation significantly influence permafrost dynamics and are challenging to incorporate in models Westerveld et al. (2023).

To conclude this discussion, even with new technologies and satellite observations, the Arctic remains significantly underrepresented in terms of observational data, particularly for subsurface measurements (Huissteden 2020). This lack of data poses challenges for statistically significant comparisons between models and observations, as well as for analyzing interactions among key components of the Arctic climate system (Liang et al. 2024).

The Arctic is currently undergoing changes and will continue to do so, even with reductions in greenhouse gas emissions. Due to its under representation in observational data, critical information about these changes is being missed. Therefore, it is urgent to mobilize a concerted effort to increase the number of Arctic observations. This study focuses on RILEs but short term events such as the first day of a sea ice-free Arctic, could occur within a few years (Heuzé & Jahn 2024). Snow variability and properties, both temporal and spatial, are particularly challenging to model, yet it affects the permafrost response Bokhorst et al. (2016). Enhanced measurements as soon as possible would be useful for snow modeling and understanding the complex interactions happening during strong sea ice changes even for short term events and not only RILEs.

Improved predictive capabilities of the permafrost response can aid risk management, particularly in regions where infrastructure stability and landslide risks depend on the permafrost state.

6 Conclusion

This master's thesis results suggest that Arctic permafrost warming during the RILE is influenced by complex interactions between atmospheric dynamics, sea ice variability, surface and ground processes. Determining whether the simulated changes are causes or consequences of the RILE is beyond the scope of this study. The findings are based on a single event modeled within a high-emission scenario, which must be considered when interpreting the results. Figure 6.1 synthesizes the key processes, highlighting regional and global implications for permafrost responses during the RILE.

The September SIE decrease (more than 5 million km^2 over 13 years) exposes open waters that absorb more SW radiation during summer and subsequently release this accumulated energy to the atmosphere in winter, primarily via SH and LH fluxes. These processes elevate TAS trends by up to 5°C per decade over the Arctic Ocean, directly influencing the TAS of adjacent land regions. This warming is further amplified by changes in atmospheric dynamics that drive colder or warmer air advection.

TAS increases over land are simulated in regions such as Nunavut, Chukotka, and the Kara Sea, with localized cooling over Siberia. The strongest warming occurs during NDJ and FMA, with trend anomalies reaching up to 5°C per decade locally and an Arctic-averaged ratio (60–90°N) of approximately 2.5 times the climatological mean during NDJ, FMA, and MJJ, and 1.5 times faster during ASO. During MJJ, warming of up to 5°C/decade is simulated in regions such as Nunavut, driven by enhanced SW radiation absorption and reduced cloud cover.

Subsurface warming is more extensive, with signals propagating to depths of 10–15 meters, reflecting the thermal inertia of the ground. At 20 cm depth (MMGST), temperature trend anomalies can reach 4°C/decade locally and are, on average, 3 times faster than the climatological mean. At 10 m depth, the average warming rate is approximately 2 times faster. The propagation of the warming signals from the surface to deeper layers introduces a lag time, with deeper signals appearing later.ALT increases are pronounced in warm permafrost margins across Eurasia, while decreases are observed in North America. These decreases may be associated with increases in LAI, though further investigation is needed. In cold, ice-rich permafrost regions, the Dzaa shows increases.

The analysis of the causes driving the simulated permafrost responses indicates that the simple SEB model accounting for snow melt energy, net LW, net SW, LH, and SH fluxes, does not directly explain the permafrost winter signal but is

correlated with the summer signal. Strong correlations with other variables, such as snow depth (especially in Chukotka), precipitation, and changes in liquid and solid soil water content, suggest the need for a more detailed SEB analysis.

In conclusion, this research indicates that RILEs may impact permafrost, with the potential to contribute to carbon release into the atmosphere. It highlights the complexity and regional variability of the processes driving permafrost warming. Additional observational data would help validate and refine model projections, particularly in remote Arctic regions, where monitoring is currently sparse. Further studies using different models and scenarios are needed to better understand the permafrost response to forcing and to apply this knowledge in climate policy, risk management, and adaptation strategies.

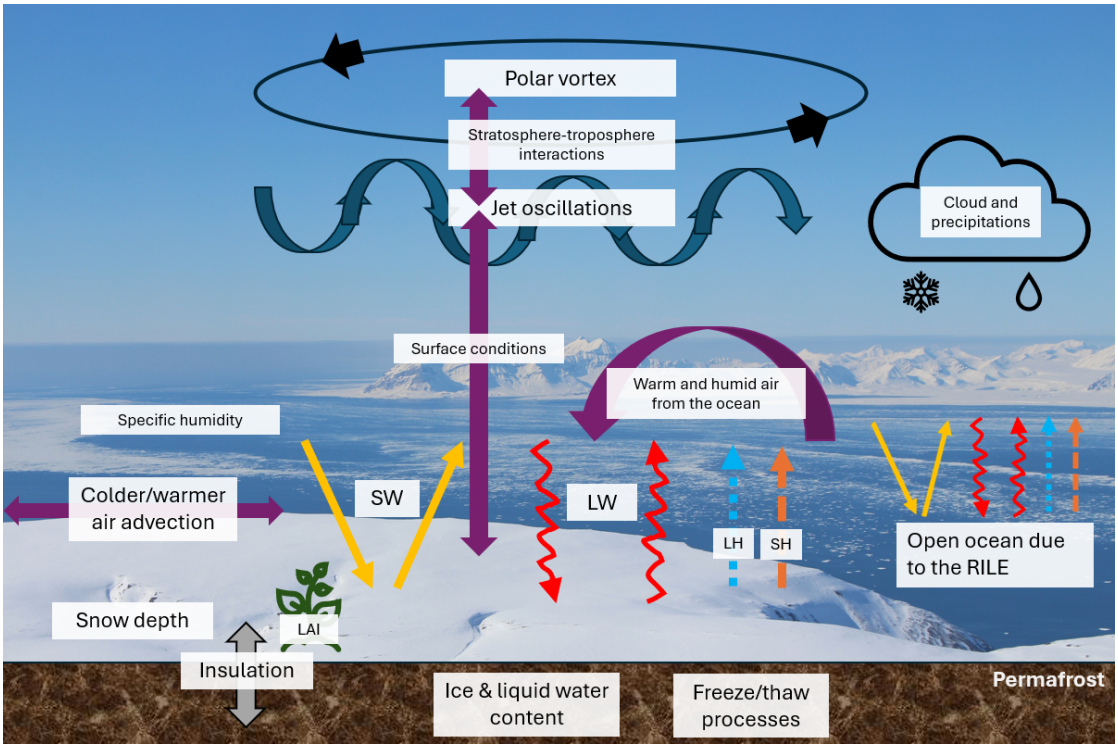


Figure 6.1: Main processes playing a role in the simulated permafrost response during the RILE 2031-2043 from CESM2-WACCM r1i1p1f1. SW: Shortwave radiation fluxes, LW: Longwave radiation fluxes, LH: Latent Heat fluxes, SH: Sensible Heat fluxes, LAI: Leaf Area Index. Credit : Antoine Paquay

Bibliography

Adakudlu, M., Andersen, J., Bakke, J., Beldring, S., Benestad, R., Bilt, W. V. D., Bogen, J., Borstad, C., Breili, K., Breivik, , Børsheim, K. Y., Christiansen, H. H., Dobler, A., Engeset, R., Frauenfelder, R., Gerland, S., Gjelten, H. M., Gundersen, J., Isaksen, K., Jaedicke, C., Kierulf, H., Kohler, J., Li, H., Lutz, J., Melvold, K., Mezghani, A., Nilsen, F., Nilsen, I. B., Nilsen, J. E. , Pavlova, O., Ravndal, O., Risebrobakken, B., Saloranta, T., Sandven, S., Schuler, T. V., Simpson, M., Skogen, M., Smedsrud, L. H., Sund, M., Vikhamar-Schuler, D., Westermann, S. & Wong, W. K. (2019), 'Climate in Svalbard 2100 – a knowledge base for climate adaptation.'. Medium: 208pp.

AMAP (2021), 'AMAP Arctic Climate Change Update 2021: Key Trends and Impacts'.

Auclair, G. & Tremblay, L. B. (2018), 'The Role of Ocean Heat Transport in Rapid Sea Ice Declines in the Community Earth System Model Large Ensemble', *Journal of Geophysical Research: Oceans* **123**(12), 8941–8957.

Barry, R. G. (2018), *Polar Environments and Global Change*, 1st ed edn, Cambridge University Press, New York, NY.

Barry, R. G. & Gan, T. Y. (2021), *The global cryosphere: past, present and future*, 2nd ed edn, Cambridge university press, Cambridge New York.

Bokhorst, S., Pedersen, S. H., Brucker, L., Anisimov, O., Bjerke, J. W., Brown, R. D., Ehrich, D., Essery, R. L. H., Heilig, A., Ingvander, S., Johansson, C., Johansson, M., Jónsdóttir, I. S., Inga, N., Luojus, K., Macelloni, G., Mariash, H., McLennan, D., Rosqvist, G. N., Sato, A., Savela, H., Schneebeli, M., Sokolov, A., Sokratov, S. A., Terzago, S., Vikhamar-Schuler, D., Williamson, S., Qiu, Y. & Callaghan, T. V. (2016), 'Changing Arctic snow cover: A review of recent developments and assessment of future needs for observations, modelling, and impacts', *Ambio* **45**(5), 516–537.

Burke, E. J., Zhang, Y. & Krinner, G. (2020), 'Evaluating permafrost physics in the Coupled Model Intercomparison Project 6 (CMIP6) models and their sensitivity to climate change', *The Cryosphere* **14**(9), 3155–3174. Publisher: Copernicus GmbH.

Böttinger, M. & Kasang, D. (n.d.), 'The SSP Scenarios'.
URL: *https://www.dkrz.de/en/communication/climate-simulations/cmip6-en/the-ssp-scenarios*

Chripko, S., Msadek, R., Sanchez-Gomez, E., Terray, L., Bessières, L. & Moine, M.-P. (2021), 'Impact of Reduced Arctic Sea Ice on Northern Hemisphere Climate and Weather in Autumn and Winter', *Journal of Climate* pp. 1–61.

Chylek, P., Folland, C., Klett, J. D., Wang, M., Hengartner, N., Lesins, G. & Dubey, M. K. (2022), 'Annual Mean Arctic Amplification 1970–2020: Observed and Simulated by CMIP6 Climate Models', *Geophysical Research Letters* **49**(13), e2022GL099371.

Danabasoglu, G., Lamarque, J., Bacmeister, J., Bailey, D. A., DuVivier, A. K., Edwards, J., Emmons, L. K., Fasullo, J., Garcia, R., Gettelman, A., Hannay, C., Holland, M. M., Large, W. G., Lauritzen, P. H., Lawrence, D. M., Lenaerts, J. T. M., Lindsay, K., Lipscomb, W. H., Mills, M. J., Neale, R., Oleson, K. W., Otto-Bliesner, B., Phillips, A. S., Sacks, W., Tilmes, S., Van Kampenhout, L., Vertenstein, M., Bertini, A., Dennis, J., Deser, C., Fischer, C., Fox-Kemper, B., Kay, J. E., Kinnison, D., Kushner, P. J., Larson, V. E., Long, M. C., Mickelson, S., Moore, J. K., Nienhouse, E., Polvani, L., Rasch, P. J. & Strand, W. G. (2020), 'The Community Earth System Model Version 2 (CESM2)', *Journal of Advances in Modeling Earth Systems* **12**(2), e2019MS001916.

Davis, N. A., Visioni, D., Garcia, R. R., Kinnison, D. E., Marsh, D. R., Mills, M., Richter, J. H., Tilmes, S., Bardeen, C. G., Gettelman, A., Glanville, A. A., MacMartin, D. G., Smith, A. K. & Vitt, F. (2023), 'Climate, Variability, and Climate Sensitivity of "Middle Atmosphere" Chemistry Configurations of the Community Earth System Model Version 2, Whole Atmosphere Community Climate Model Version 6 (CESM2(WACCM6))', *Journal of Advances in Modeling Earth Systems* **15**(9), e2022MS003579.

DeRepentigny, P., Jahn, A., Holland, M. M. & Smith, A. (2020), 'Arctic Sea Ice in Two Configurations of the CESM2 During the 20th and 21st Centuries', *Journal of Geophysical Research: Oceans* **125**(9), e2020JC016133.

Döscher, R. & Koenigk, T. (2013), 'Arctic rapid sea ice loss events in regional coupled climate scenario experiments', *Ocean Science* **9**(2), 217–248. Publisher: Copernicus GmbH.

Eyring, V., Bony, S., Meehl, G. A., Senior, C. A., Stevens, B., Stouffer, R. J. & Taylor, K. E. (2016), 'Overview of the Coupled Model Intercomparison Project Phase 6 (CMIP6) experimental design and organization', *Geoscientific Model Development* **9**(5), 1937–1958.

Gettelman, A., Mills, M. J., Kinnison, D. E., Garcia, R. R., Smith, A. K., Marsh, D. R., Tilmes, S., Vitt, F., Bardeen, C. G., McInerny, J., Liu, H., Solomon, S. C., Polvani, L. M., Emmons, L. K., Lamarque, J., Richter, J. H., Glanville, A. S., Bacmeister, J. T., Phillips, A. S., Neale, R. B., Simpson, I. R., DuVivier, A. K., Hodzic, A. & Randel, W. J. (2019), 'The Whole Atmosphere Community Climate Model Version 6 (WACCM6)', *Journal of Geophysical Research: Atmospheres* **124**(23), 12380–12403.

Goosse, H., Kay, J. E., Armour, K. C., Bodas-Salcedo, A., Chepfer, H., Docquier, D., Jonko, A., Kushner, P. J., Lecomte, O., Massonnet, F., Park, H.-S., Pithan, F., Svensson, G. & Vancoppenolle, M. (2018), 'Quantifying climate feedbacks in polar regions', *Nature Communications* **9**(1), 1919.

Heuzé, C. & Jahn, A. (2024), 'The first ice-free day in the Arctic Ocean could occur before 2030', *Nature Communications* **15**(1), 10101.

Hodson, T. O. (2022), 'Root-mean-square error (RMSE) or mean absolute error (MAE): when to use them or not', *Geoscientific Model Development* **15**(14), 5481–5487. Publisher: Copernicus GmbH.

Hoelzle, M., Hauck, C., Mathys, T., Noetzli, J., Pellet, C. & Scherler, M. (2022), 'Long-term energy balance measurements at three different mountain permafrost sites in the Swiss Alps', *Earth System Science Data* **14**(4), 1531–1547.

Holland, M. M., Bitz, C. M. & Tremblay, B. (2006), 'Future abrupt reductions in the summer Arctic sea ice', *Geophysical Research Letters* **33**(23), 2006GL028024.

Huissteden, J. v. (2020), *Thawing permafrost: permafrost carbon in a warming arctic*, Springer, Cham, Switzerland.

IPCC (2023), *Climate Change 2022 – Impacts, Adaptation and Vulnerability: Working Group II Contribution to the Sixth Assessment Report of the Intergovernmental Panel on Climate Change*, 1 edn, Cambridge University Press.

Jahn, A., Holland, M. M. & Kay, J. E. (2024), 'Projections of an ice-free Arctic Ocean', *Nature Reviews Earth & Environment* **5**(3), 164–176. Publisher: Nature Publishing Group.

Lawrence, D. M., Fisher, R. A., Koven, C. D., Oleson, K. W., Swenson, S. C., Bonan, G., Collier, N., Ghimire, B., Van Kampenhout, L., Kennedy, D., Kluzek, E., Lawrence, P. J., Li, F., Li, H., Lombardozzi, D., Riley, W. J., Sacks, W. J., Shi, M., Vertenstein, M., Wieder, W. R., Xu, C., Ali, A. A., Badger, A. M., Bisht, G., Van Den Broeke, M., Brunke, M. A., Burns, S. P., Buzan, J., Clark, M., Craig, A., Dahlin, K., Drewniak, B., Fisher, J. B., Flanner, M., Fox, A. M., Gentine, P., Hoffman, F., Keppel-Aleks, G., Knox, R., Kumar, S., Lenaerts, J., Leung, L. R., Lipscomb, W. H., Lu, Y., Pandey, A., Pelletier, J. D., Perket, J., Randerson, J. T., Ricciuto, D. M., Sanderson, B. M., Slater, A., Subin, Z. M., Tang, J., Thomas, R. Q., Val Martin, M. & Zeng, X. (2019), 'The Community Land Model Version 5: Description of New Features, Benchmarking, and Impact of Forcing Uncertainty', *Journal of Advances in Modeling Earth Systems* **11**(12), 4245–4287.

Lawrence, D. M., Fisher, R., Koven, C., Oleson, K. W., Swenson, S., Vertenstein, M., Bonan, G., Levis, S., Kluzek, E., Lawrence, P. J., Lombardozzi, D., Riley, W. J., Wieder, W. R., Xia, Y. & Zeng, X. (2020), Technical description of version 5.0 of the community land model (clm5.0), Technical report, National Center for Atmospheric Research (NCAR), Boulder, Colorado, USA. Accessed January 2025.

Lawrence, D. M., Slater, A. G., Tomas, R. A., Holland, M. M. & Deser, C. (2008), 'Accelerated Arctic land warming and permafrost degradation during rapid sea ice loss', *Geophysical Research Letters* **35**(11). _eprint: https://onlinelibrary.wiley.com/doi/pdf/10.1029/2008GL033985.

Leys, C., Ley, C., Klein, O., Bernard, P. & Licata, L. (2013), 'Detecting outliers: Do not use standard deviation around the mean, use absolute deviation around the median', *Journal of Experimental Social Psychology* **49**(4), 764–766.

Liang, Y.-C., Kwon, Y.-O., Frankignoul, C., Gastineau, G., Smith, K. L., Polvani, L. M., Sun, L., Peings, Y., Deser, C., Zhang, R. & Screen, J. (2024), 'The Weakening of the Stratospheric Polar Vortex and the Subsequent Surface Impacts as Consequences to Arctic Sea Ice Loss', *Journal of Climate* **37**(1), 309–333.

Liu, Y., Tang, Q., Zhang, C., Chen, D., Francis, J. A., Leung, L. R. & Chen, H. W. (2024), 'The disproportionate impact of enhanced evaporation from melting arctic sea ice on cold-season land precipitation trends', *npj Climate and Atmospheric Science* **7**(1), 126.

Marshall, S. (2012), *The cryosphere*, Princeton primers in climate, Princeton University Press, Princeton, N.J.

NASA/JPL-Caltech (2023), 'Graphic: Major Greenhouse Gas Sources, Lifespans, and Possible Added Heat - NASA Science'.
URL: *https://science.nasa.gov/resource/graphic-major-greenhouse-gas-sources-lifespans-and-possible-added-heat/*

Notz, D. & Community, S. (2020), 'Arctic Sea Ice in CMIP6', *Geophysical Research Letters* **47**(10), e2019GL086749.

NSIDC (2024), 'Data Tools'.
URL: *https://nsidc.org/sea-ice-today/sea-ice-tools*

NSIDC (n.d.*a*), 'Science of Sea Ice'.
URL: *https://nsidc.org/learn/parts-cryosphere/sea-ice/science-sea-ice*

NSIDC (n.d.*b*), 'Why Frozen Ground Matters'.
URL: *https://nsidc.org/learn/parts-cryosphere/frozen-ground-permafrost/why-frozen-ground-matters*

Obu, J., Westermann, S., Barboux, C., Bartsch, A., Delaloye, R., Grosse, G., Heim, B., Hugelius, G., Irrgang, A., Kääb, A. M., Kroisleitner, C., Matthes, H., Nitze, I., Pellet, C., Seifert, F. M., Strozzi, T., Wegmüller, U., Wieczorek, M. & Wiesmann, A. (2021), 'ESA Permafrost Climate Change Initiative (Permafrost_cci): Permafrost extent for the Northern Hemisphere, v3.0'.
URL: *https://catalogue.ceda.ac.uk/uuid/6e2091cb0c8b4106921b63cd5357c97c*

Oleson, K. W., Niu, G.-Y., Yang, Z.-L., Lawrence, D. M., Thornton, P. E., Lawrence, P. J., Stockli, R., Dickinson, R. E., Bonan, G. B. & Levis, S. (2007), Technical description of version 3.5 of the community land model (clm3.5), Technical report, National Center for Atmospheric Research (NCAR), Boulder, Colorado, USA. Accessed January 2025.

O'Neill, B. C., Tebaldi, C., Van Vuuren, D. P., Eyring, V., Friedlingstein, P., Hurtt, G., Knutti, R., Kriegler, E., Lamarque, J.-F., Lowe, J., Meehl, G. A., Moss, R., Riahi, K. & Sanderson, B. M. (2016), 'The Scenario Model Intercomparison Project (ScenarioMIP) for CMIP6', *Geoscientific Model Development* **9**(9), 3461–3482.

Paquin, J.-P., Döscher, R., Sushama, L. & Koenigk, T. (2013), 'Causes and consequences of mid–21st-century rapid ice loss events simulated by the Rossby centre regional atmosphere-ocean model', *Tellus A: Dynamic Meteorology and Oceanography* **65**(1).

Rantanen, M., Karpechko, A. Y., Lipponen, A., Nordling, K., Hyvärinen, O., Ruosteenoja, K., Vihma, T. & Laaksonen, A. (2022), 'The Arctic has warmed

nearly four times faster than the globe since 1979', *Communications Earth & Environment* **3**(1), 1–10. Publisher: Nature Publishing Group.

Razali, N. M. & Wah, Y. B. (2011), 'Power Comparisons of Shapiro-Wilk, Kolmogorov-Smirnov, Lilliefors and Anderson-Darling Tests.', *Journal of Statistical Modeling and Analytics* **2**(1), 21–33.

Rieke, O., Årthun, M. & Dörr, J. S. (2023), 'Rapid sea ice changes in the future Barents Sea', *The Cryosphere* **17**(4), 1445–1456.

Sedgwick, P. (2014), 'Spearman's rank correlation coefficient', *BMJ* p. g7327.

Serreze, M. C. & Barry, R. G. (2011), 'Processes and impacts of Arctic amplification: A research synthesis', *Global and Planetary Change* **77**(1), 85–96.

Serreze, M. C. & Barry, R. G. (2014), *The Arctic climate system*, Cambridge atmospheric and space science series, 2nd ed edn, Cambridge university press, New York.

Smith, S. L., O'Neill, H. B., Isaksen, K., Noetzli, J. & Romanovsky, V. E. (2022), 'The changing thermal state of permafrost', *Nature Reviews Earth & Environment* **3**(1), 10–23.

Sticker, A. (2022), Analyse des événements de fonte rapide de la glace de mer arctique dans le cadre du réchauffement global : inventaire et mécanismes., PhD thesis, Faculté des sciences, Université catholique de Louvain.
URL: *http://hdl.handle.net/2078.1/thesis:34757*

Van Vliet-Lanoë, B. (2014), *Les environnements froids: glaciaire et périglaciaire cours et exercices corrigés master sciences de la terre sciences de l'environnement*, Vuibert, Paris.

Vavrus, S., Holland, M. M. & Bailey, D. A. (2011), 'Changes in Arctic clouds during intervals of rapid sea ice loss', *Climate Dynamics* **36**(7-8), 1475–1489.

Westerveld, L., Kurvits, T., Schoolmeester, T., Eckhoff, T. S., Overduin, P. P., Fritz, M., Alfthan, B., Sinisalo, A. & Alfred Wegner Institute (2023), *Arctic Permafrost Atlas*, first edn, GRID-Arendal.

Zar, J. H. (1972), 'Significance Testing of the Spearman Rank Correlation Coefficient', *Journal of the American Statistical Association* **67**(339), 578–580.

Zhang, T. (2005), 'Influence of the seasonal snow cover on the ground thermal regime: An overview', *Reviews of Geophysics* **43**(4). _eprint: https://onlinelibrary.wiley.com/doi/pdf/10.1029/2004RG000157.

Zuo, B., Li, J., Sun, C. & Zhou, X. (2019), 'A new statistical method for detecting trend turning', *Theoretical and Applied Climatology* **138**(1-2), 201–213.

List of Figures

1.1 Arctic September sea ice extent based on satellite observations. Credit: NSIDC/NASA 2

2.1 Impacts of the polar vortex stability on the jet stream behavior and warm/cold air advection. Credit: NOAA Climate.gov 8

2.2 Current modelled Arctic permafrost coverage. Credit: Westerveld et al. (2023) 9

2.3 Annual temperature variations from the surface to below the permafrost, showing the Active Layer Thickness (ALT) indicating seasonal thaw depth and the Depth of zero annual amplitude (Dzaa) marks the depth where seasonal temperature fluctuations cease. Credit: Burke et al. (2020) 10

2.4 « (a) Composite anomaly time series of September sea ice extent (solid line) and OND Tair (dashed line) over Arctic land area (65°–80°N, 60°–300°E). Composites are formed by averaging nine 31-yr anomaly time series. Each of the nine time series are centered about the mid-point of a CCSM3 rapid sea ice loss event (lag 0 years) and are anomalies from the lag 10 to 5 year mean. (b) Average monthly Arctic land air temperature trends during rapid sea ice loss periods and outside sea ice loss periods. The difference in trends are statistically significant at the 90% (single asterisk) and 95% (double asterisk) levels. (c) Maps of air temperature trends for OND during and outside abrupt sea ice loss periods.» (Lawrence et al. 2008) Credit: Lawrence et al. (2008) 13

3.1 Evolution of the greenhouse-gas induced radiative forcing under different Shared Socioeconomic Pathways (SSPs) in the Coupled Model Intercomparison Project Phase 6 (CMIP6). Credit : Böttinger & Kasang (n.d.) based on O'Neill et al. (2016). 17

3.2 Selected regions for the analysis. 22

4.1 September Sea Ice Extent (SIE) in ensemble member r1i1p1f1 from CESM2-WACCM (the blue solid line is the 5 year rolling mean) compared with satellite SIE observations from NSIDC (2024). . . . 23

4.2 Modeled permafrost extent based on the Dzaa temperature distribution for 2015–2019 from CESM2-WACCM, showing the -2°C isotherm (green line) and areas of warm and cold permafrost. Observational data from Obu et al. (2021) representing discontinuous and continuous permafrost margins in blue and red, respectively. . . 24

4.3 Seasonal near-surface (2m) air temperature (TAS) and snow depth (SND) trend anomalies during the RILE 2031-2043 of the r1i1p1f1 ensemble member of CESM2-WACCM. Green dots are the significant anomalies using a t-test and a p-value threshold of 0.05. The trend anomaly is the difference of the linear trend during the RILE 2031-2043 and the trend of a centered climatological mean 2023-2053 of three RILE free ensemble members (r2i1p1f1, r4i1p1f1 and r5i1p1f1). 26

4.4 Seasonal permafrost trend anomalies of MMGST (Mean Monthly Ground Temperature at 20cm depth), GT10m (Ground Temperature at 10m) and SO (Surface Offset) during the RILE 2031-2043 from CESM2-WACCM r1i1p1f1. Green dots are the significant anomalies using a t-test and a p-value threshold of 0.05. 29

4.5 Annual permafrost trend anomalies of ALT (Active Layer Thickness, maximun annual thaw depth) and Dzaa (Depth of zero annual amplitude) during the RILE 2031-2043 from CESM2-WACCM r1i1p1f1. Green dots are the significant anomalies using a t-test and a p-value threshold of 0.05. 30

4.6 Arctic permafrost monthly trend anomalies of ground temperatures during the RILE 2031-2043 from CESM2-WACCM r1i1p1f1. The green line is the total area of permafrost for each latitudes and the dashed red line is the +/- 1°C trend anomaly isotherm. 32

4.7 Regional permafrost monthly trend anomalies of ground temperatures during the RILE 2031-2043 from CESM2-WACCM r1i1p1f1. Green dots are the significant anomalies using a t-test and a p-value threshold of 0.05. Refer to figure 3.2 for region definitions. 33

4.8 Arctic and regional annual average time series of ALT (Active Layer Thickness, maximum annual thaw depth), Dzaa (Depth of zero annual amplitude), SO (Surface Offset), snow depth, surface air temperature, ground temperature at 10m, permafrost extent and MAGST (Mean Annual Ground Surface Temperature at 0.2m) from CESM2-WACCM r1i1p1f1 (solid line) and average of r2i1p1f1/r4i1p1f1/r5i1p1f1 (dashed line). Red boxes are RILE periods r1i1p1f1 (2022-2027 and 2031-2043). Refer to figure 3.2 for region definitions. The exact trend values during the RILE 2031-2043 and the significance of the difference with the climatological trend average can be found in the appendix (Table A.1). 35

4.9 Arctic and regional annual average correlation between September SIE (Sea Ice Extent) and ALT (Active Layer Thickness, maximum annual thaw depth), Dzaa (Depth of zero annual amplitude), SO (Surface Offset), Snd (snow depth), Tas (surface air temperature), GT 10m (ground temperature at 10m), permafrost extent and MMGST (Mean Annual Ground Surface Temperature at 0.2m) from CESM2-WACCM r1i1p1f1. Red boxes are RILE periods r1i1p1f1 (2022-2027 and 2031-2043). Green dots are significant (p-value < 0.05) Pearson correlations. The y axis unit is the Pearson correlation coefficient, -1 means perfectly negatively correlated and +1, perfectly positively correlated. Refer to figure 3.2 for region definitions. 36

4.10 Seasonal sea ice concentration difference between the start and the end of the RILE 2031-2043 from CESM2-WACCM r1i1p1f1. 37

4.11 Spearman correlation coefficient and significance (black stars, p-value threshold = 0.05) between permafrost soil temperature trend anomalies at a depth of 20 cm and trend anomalies of other variables. The variable SEB represents the surface energy balance. Trend anomalies are calculated as the difference between the trends during the RILE period (2031–2043) and the trends during the centered climatological mean period (2023–2053) in the CESM2-WACCM climate model 42

6.1 Main processes playing a role in the simulated permafrost response during the RILE 2031-2043 from CESM2-WACCM r1i1p1f1. SW: Shortwave radiation fluxes, LW: Longwave radiation fluxes, LH: Latent Heat fluxes, SH: Sensible Heat fluxes, LAI: Leaf Area Index. Credit : Antoine Paquay 47

A.1 Seasonal trends from the CESM2-WACCM model during the RILE period (2031–2043) and the climatological average (2023–2053), along with the ratio between the two. TAS refers to surface air temperature at 2 m; MMGST is the mean monthly ground temperature at 20 cm depth; GT10m is the ground temperature at 10 m depth; SND represents snow depth; and SO is the surface offset. Black stars on the ratio bars indicate statistical significance (p-value threshold = 0.05) of the difference, calculated using an adapted t-test. 62

A.2 Seasonal trend differences from the CESM2-WACCM model between the RILE period (2031–2043) and the climatological average (2023–2053). LH refers to the surface latent heat flux (positive upward); SH is the surface sensible heat flux (positive upward); SWnet represents the net shortwave radiation (positive downward); and LWnet is the net longwave radiation (positive downward). Green stars indicate statistical significance (p-value threshold = 0.05) of the difference, calculated using an adapted t-test. 63

A.3 Seasonal trend differences from the CESM2-WACCM model between the RILE period (2031–2043) and the climatological average (2023–2053). SST refers to sea surface temperature; LAI is the leaf area index; mrfso represents the total frozen water content in the soil across all depths; and mrlso is the total liquid water content in the soil across all depths. Green stars indicate statistical significance (p-value threshold = 0.05) of the difference, calculated using an adapted t-test. 64

A.4 Seasonal trend differences from the CESM2-WACCM model between the RILE period (2031–2043) and the climatological average (2023–2053). SEB refers to the surface energy balance (at the lower boundary of the atmosphere); clt represents the total cloud cover percentage; QM is the snow melt energy flux related to latent heat; and pr includes both liquid and solid precipitation. Green stars indicate statistical significance (p-value threshold = 0.05) of the difference, calculated using an adapted t-test. 65

A.5 Seasonal trend differences from the CESM2-WACCM model between the RILE period (2031–2043) and the climatological average (2023–2053). PSL refers to the sea level pressure; TAS represents the surface air temperature at 2 m; UA is the zonal wing at 200 hPa; and VA is the meridional wind at 200 hPa. Green stars indicate statistical significance (p-value threshold = 0.05) of the difference, calculated using an adapted t-test. 66

A.6 Monthly trend differences of the zonal wind from the CESM2-WACCM model between the RILE period (2031–2043) and the climatological average (2023–2053). Green stars indicate statistical significance (p-value threshold = 0.05) of the difference, calculated using an adapted t-test. 67

A.7 Monthly trend differences of the air temperature from the CESM2-WACCM model between the RILE period (2031–2043) and the climatological average (2023–2053). Green stars indicate statistical significance (p-value threshold = 0.05) of the difference, calculated using an adapted t-test. 68

List of Tables

3.1 CESM2-WACCM characteristics. 16

A.1 Arctic and regional annual trends and trend anomalies of ALT (Active Layer Thickness, maximum annual thaw depth), Dzaa (Depth of zero annual amplitude), SO (Surface Offset), snow depth, surface air temperature, ground temperature at 10m, permafrost extent and MAGST (Mean Annual Ground Surface Temperature at 0.2m) from CESM2-WACCM r1i1p1f1 RILE 2031-2043 period (X RILE) and average of r2i1p1f1/r4i1p1f1/r5i1p1f1 2023-2053 period (X mean). Refer to figure 3.2 for region definitions. P-values of the t-test are in green (≤ 0.05), orange (0.06-0.09) and red (≥ 0.1). 61

Appendix

Variables	Nunavut	Svalbard	Chukotka	Alaska	Kara Sea	Global Arctic	
Tas RILE	0,24	0,26	0,24	0,13	0,26	0,17	°C/year
Tas mean	0,11	0,11	0,09	0,08	0,11	0,08	
Anomaly	0,13	0,15	0,14	0,05	0,15	0,09	
P-Value	0,06	0,12	0,06	0,64	0,05	0,01	
Snd RILE	0,00	0,01	0,00	0,00	0,00	0,00	m/year
Snd mean	0,00	0,00	0,00	0,00	0,00	0,00	
Anomaly	0,00	0,01	0,00	0,00	0,00	0,00	
P-Value	0,09	0,01	0,61	0,18	0,61	0,38	
SO RILE	-0,09	0,17	-0,05	0,04	-0,03	-0,03	°C/year
SO mean	0,03	0,10	-0,01	0,05	-0,01	0,00	
Anomaly	-0,11	0,06	-0,04	-0,01	-0,02	-0,02	
P-Value	0,02	0,36	0,40	0,87	0,59	0,15	
MAGST RILE	0,22	0,10	0,27	0,13	0,31	0,20	°C/year
MAGST mean	0,08	0,01	0,10	0,03	0,12	0,08	
Anomaly	0,14	0,09	0,17	0,10	0,19	0,13	
P-Value	0,00	0,05	0,01	0,18	0,00	0,00	
ALT RILE	0,04	0,02	0,14	0,08	0,06	0,08	m/year
ALT mean	0,01	0,00	0,07	0,04	0,02	0,03	
Anomaly	0,02	0,02	0,08	0,04	0,04	0,05	
P-Value	0,02	0,03	0,00	0,45	0,02	0,00	
GT 10m RILE	0,12	0,03	0,15	0,05	0,18	0,12	°C/year
GT 10m mean	0,07	0,01	0,08	0,01	0,08	0,06	
Anomaly	0,05	0,03	0,07	0,04	0,10	0,06	
P-Value	0,00	0,01	0,00	0,02	0,00	0,00	
Dzaa RILE	0,75	0,04	0,27	-0,07	0,99	0,51	m/year
Dzaa mean	0,05	0,16	0,08	0,09	0,03	0,06	
Anomaly	0,69	-0,12	0,19	-0,15	0,96	0,45	
P-Value	0,00	0,28	0,46	0,34	0,03	0,00	
PE RILE	-54705	-102	-2401	-8868	-18482	-170206	km^2/year
PE mean	-4385	45	-2631	-12339	-2579	-87169	
Anomaly	-50320	-147	230	3471	-15903	-83036	
P-Value	0,01	0,03	0,74	0,06	0,01	0,01	

Table A.1: Arctic and regional annual trends and trend anomalies of ALT (Active Layer Thickness, maximum annual thaw depth), Dzaa (Depth of zero annual amplitude), SO (Surface Offset), snow depth, surface air temperature, ground temperature at 10m, permafrost extent and MAGST (Mean Annual Ground Surface Temperature at 0.2m) from CESM2-WACCM r1i1p1f1 RILE 2031-2043 period (X RILE) and average of r2i1p1f1/r4i1p1f1/r5i1p1f1 2023-2053 period (X mean). Refer to figure 3.2 for region definitions. P-values of the t-test are in green (≤ 0.05), orange (0.06-0.09) and red (≥ 0.1).

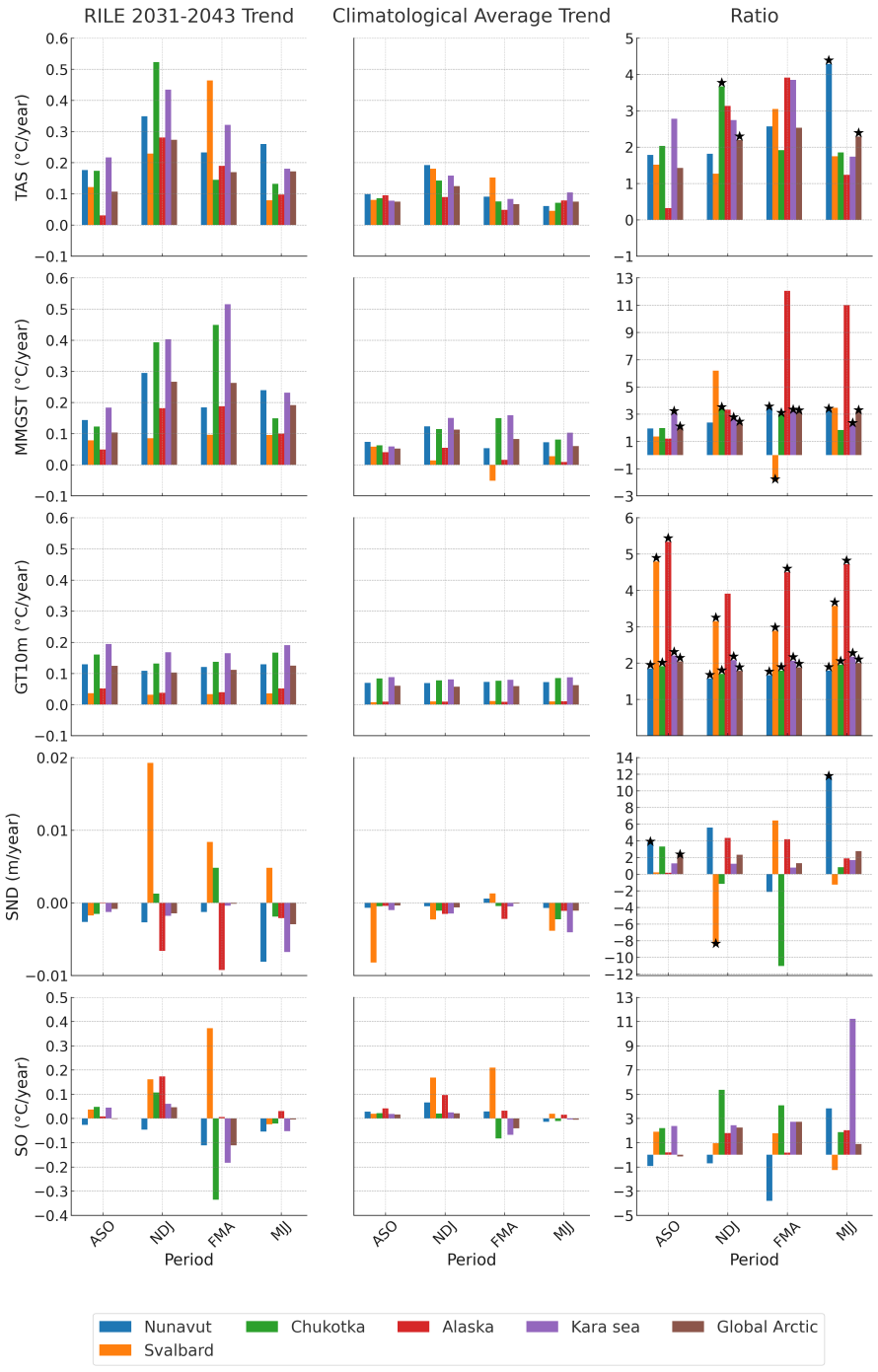


Figure A.1: Seasonal trends from the CESM2-WACCM model during the RILE period (2031–2043) and the climatological average (2023–2053), along with the ratio between the two. TAS refers to surface air temperature at 2 m; MMGST is the mean monthly ground temperature at 20 cm depth; GT10m is the ground temperature at 10 m depth; SND represents snow depth; and SO is the surface offset. Black stars on the ratio bars indicate statistical significance (p-value threshold = 0.05) of the difference, calculated using an adapted t-test.

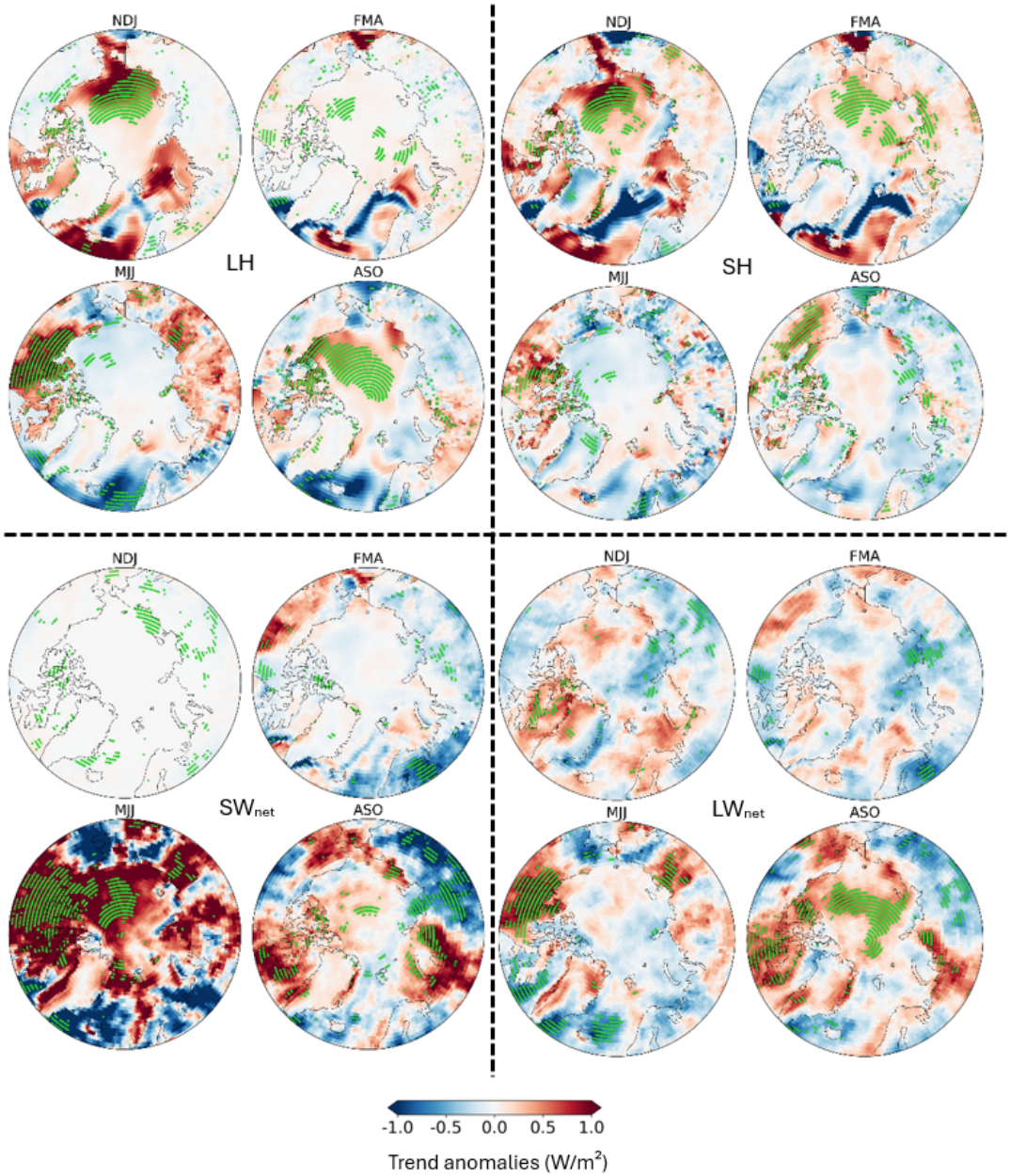


Figure A.2: Seasonal trend differences from the CESM2-WACCM model between the RILE period (2031–2043) and the climatological average (2023–2053). LH refers to the surface latent heat flux (positive upward); SH is the surface sensible heat flux (positive upward); SWnet represents the net shortwave radiation (positive downward); and LWnet is the net longwave radiation (positive downward). Green stars indicate statistical significance (p-value threshold = 0.05) of the difference, calculated using an adapted t-test.

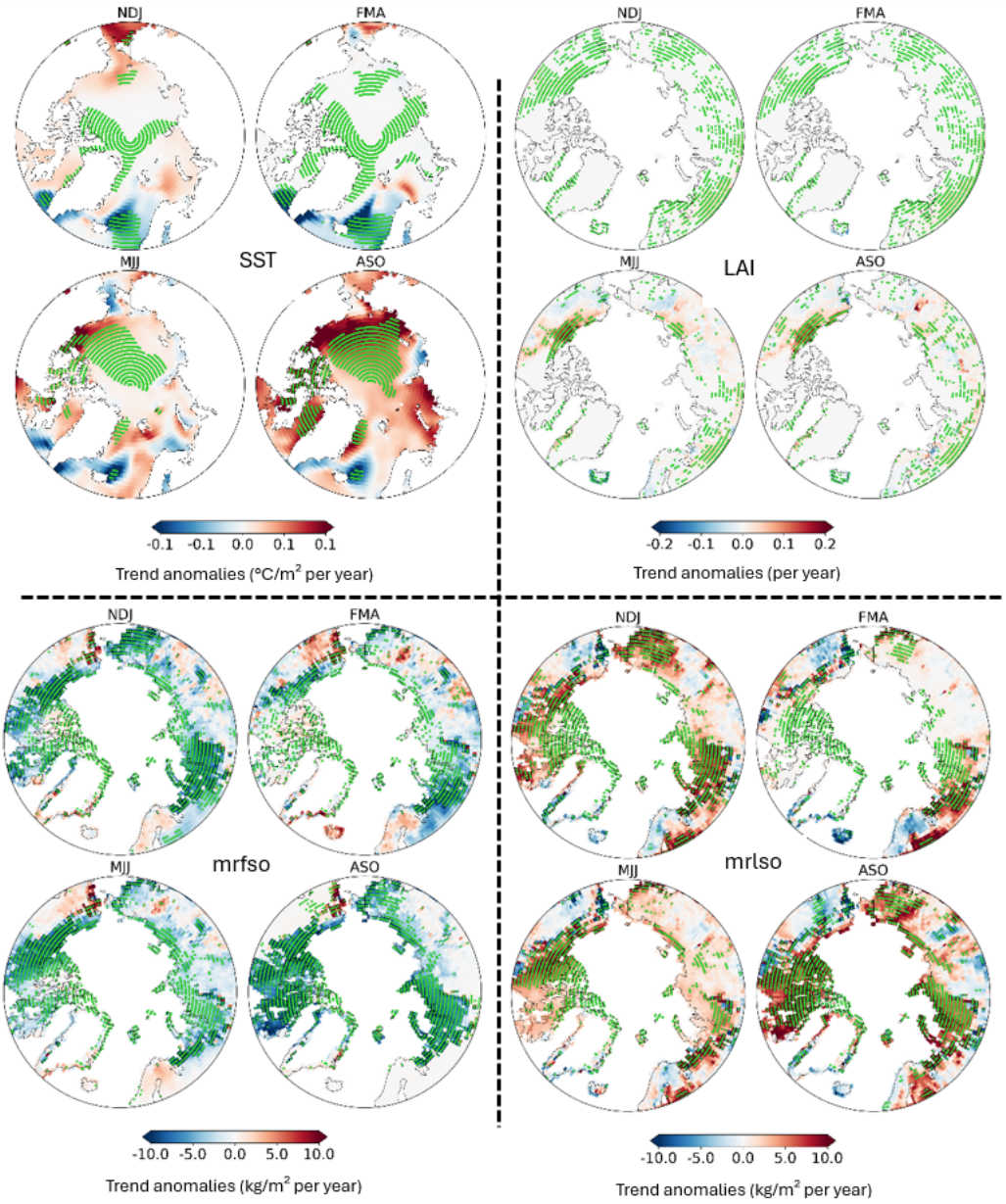


Figure A.3: Seasonal trend differences from the CESM2-WACCM model between the RILE period (2031–2043) and the climatological average (2023–2053). SST refers to sea surface temperature; LAI is the leaf area index; mrfso represents the total frozen water content in the soil across all depths; and mrlso is the total liquid water content in the soil across all depths. Green stars indicate statistical significance (p-value threshold = 0.05) of the difference, calculated using an adapted t-test.

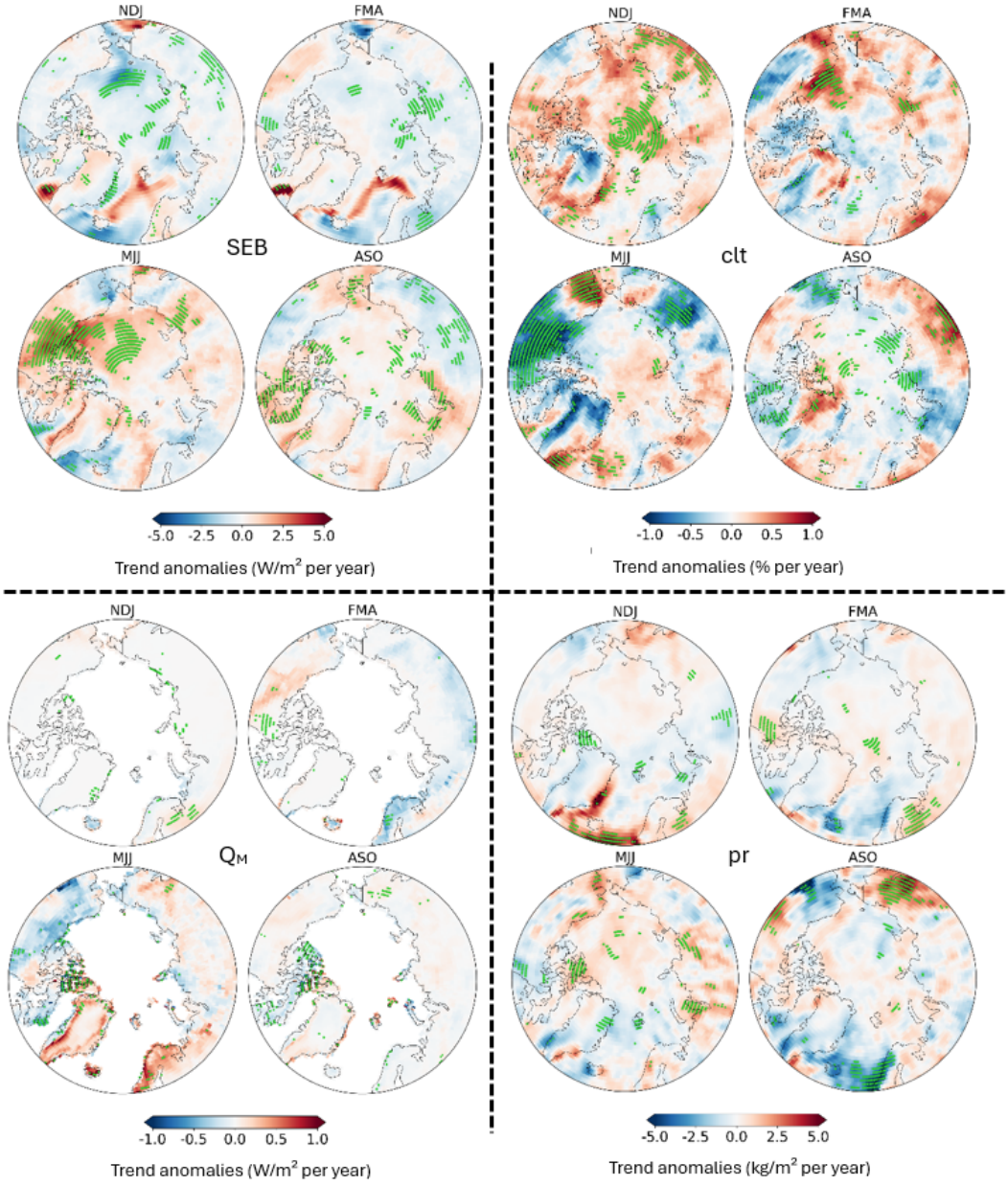


Figure A.4: Seasonal trend differences from the CESM2-WACCM model between the RILE period (2031–2043) and the climatological average (2023–2053). SEB refers to the surface energy balance (at the lower boundary of the atmosphere); clt represents the total cloud cover percentage; QM is the snow melt energy flux related to latent heat; and pr includes both liquid and solid precipitation. Green stars indicate statistical significance (p-value threshold = 0.05) of the difference, calculated using an adapted t-test.

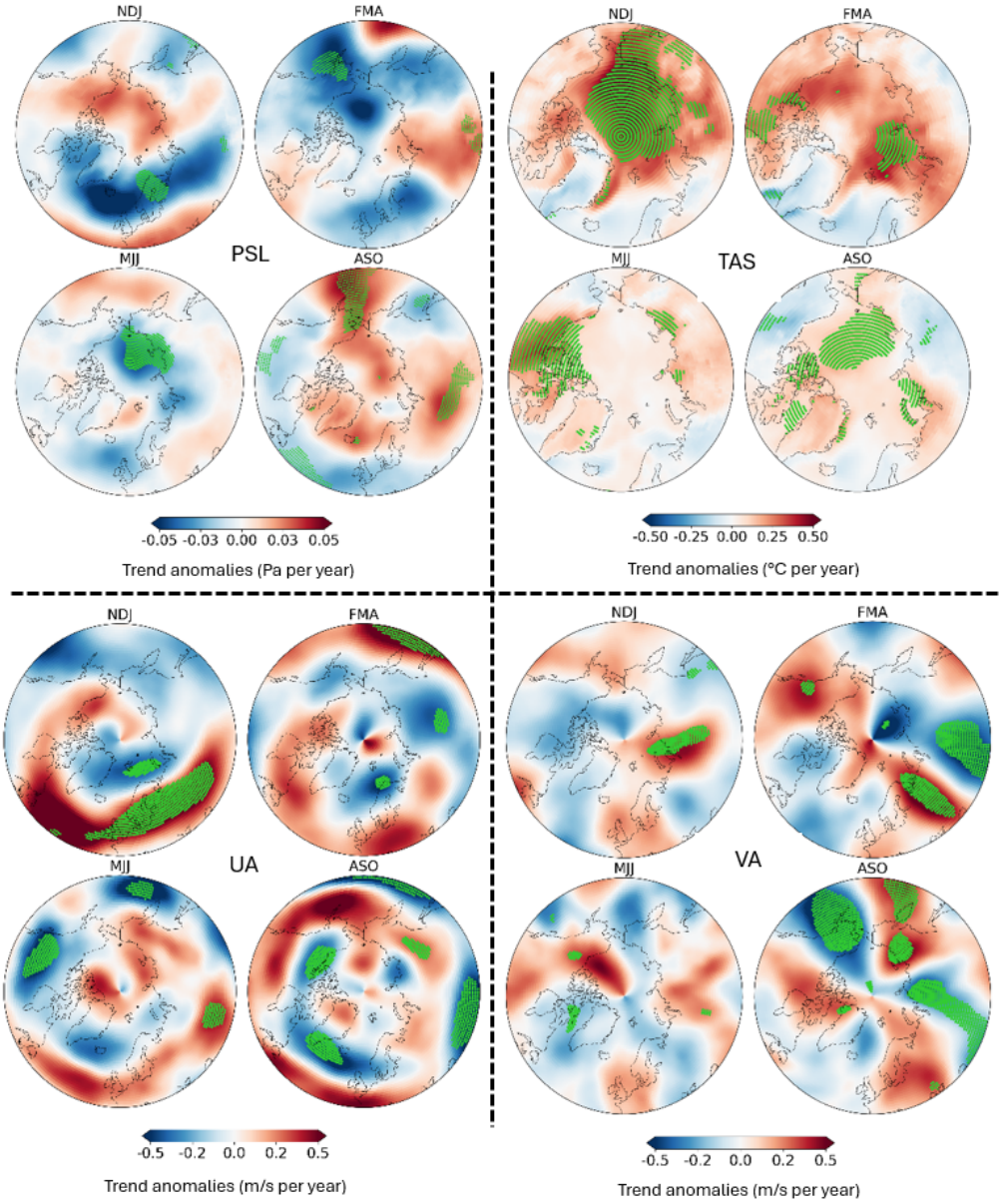


Figure A.5: Seasonal trend differences from the CESM2-WACCM model between the RILE period (2031–2043) and the climatological average (2023–2053). PSL refers to the sea level pressure; TAS represents the surface air temperature at 2 m; UA is the zonal wing at 200 hPa; and VA is the meridional wind at 200 hPa. Green stars indicate statistical significance (p-value threshold = 0.05) of the difference, calculated using an adapted t-test.

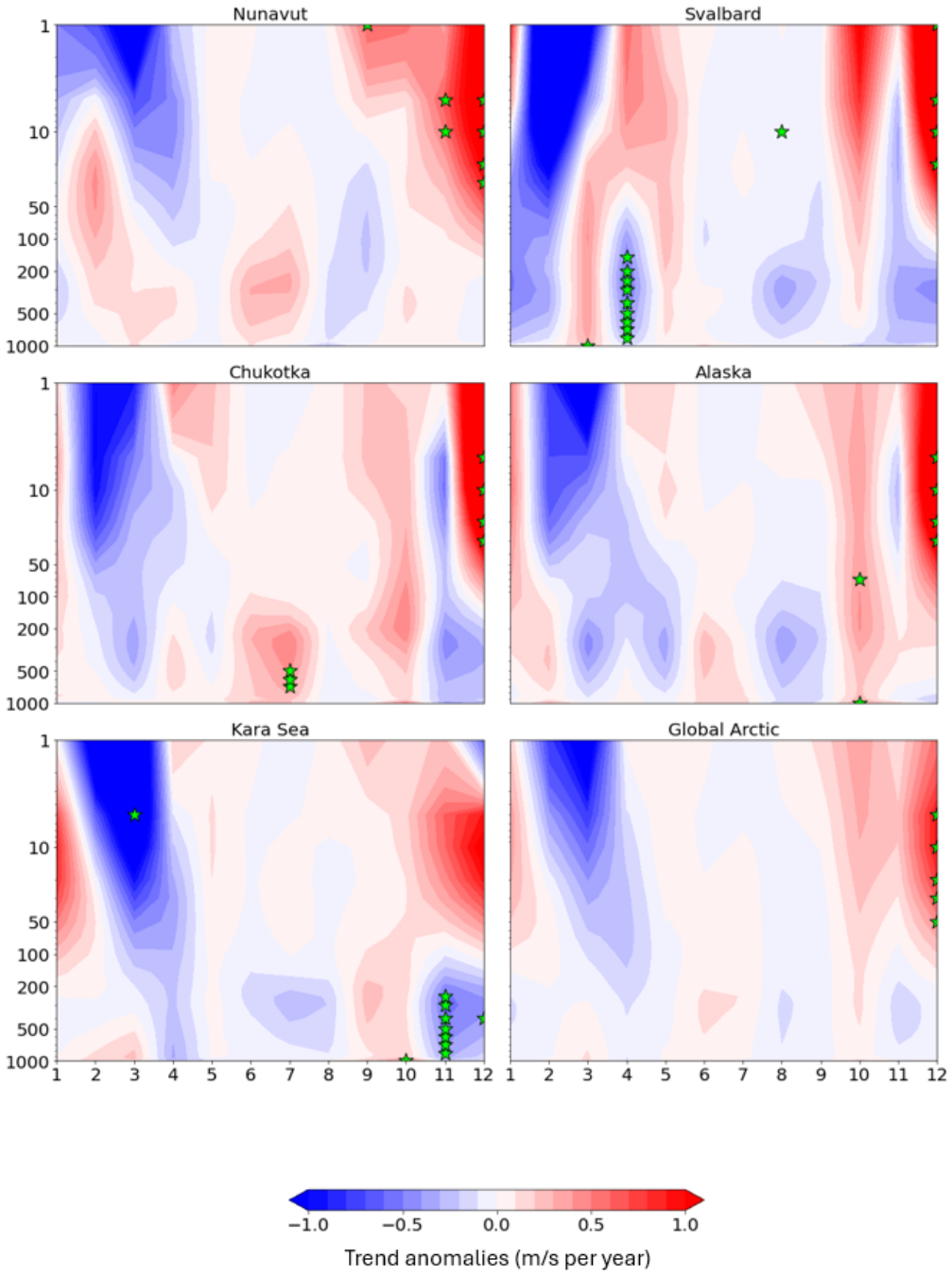


Figure A.6: Monthly trend differences of the zonal wind from the CESM2-WACCM model between the RILE period (2031–2043) and the climatological average (2023–2053). Green stars indicate statistical significance (p-value threshold = 0.05) of the difference, calculated using an adapted t-test.

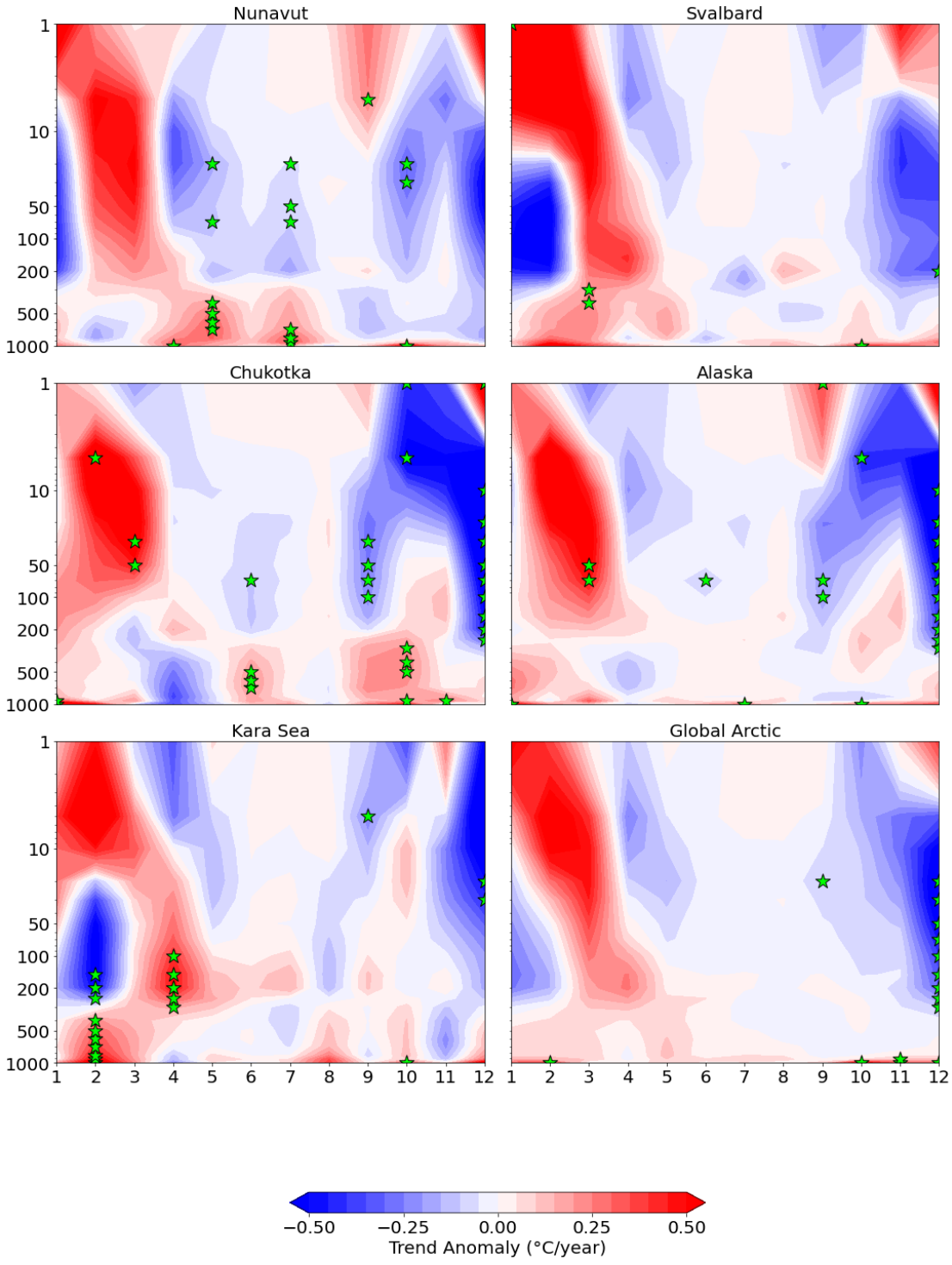


Figure A.7: Monthly trend differences of the air temperature from the CESM2-WACCM model between the RILE period (2031–2043) and the climatological average (2023–2053). Green stars indicate statistical significance (p-value threshold = 0.05) of the difference, calculated using an adapted t-test.

Curriculum vitae

- **Collège Saint-Barthélemy, Liège** Mathematics and Sciences option (2011–2017)
- **First year of the bachelor in Bioengineering, UCLouvain** (2017–2018)
- **Bachelor in Geography, UCLouvain** (2018–2022)
- **Master in Geography - Climatology Research Focus, UCLouvain** Including an Erasmus exchange at the University of Oslo (Spring Semester 2023) (2022–2025)
- **Master Courses at UNIS (The University Centre in Svalbard)**
  - **AS-304**: Risk Handling in Arctic Operations (2023)
  - **AG-342**: The Marine Cryosphere and its Cenozoic History (2024)

UNIVERSITÉ CATHOLIQUE DE LOUVAIN
Faculté des sciences
Place des Sciences, 2 bte L6.06.01, 1348 Louvain-la-Neuve, Belgique | www.uclouvain.be/sc